




The Stubenberg meteorite—An LL6 chondrite fragmental breccia recovered soon after precise prediction of the strewn field

Addi BISCHOFF^{1,*} , Jean-Alix BARRAT², Kerstin BAUER³, Christoph BURKHARDT¹, Henner BUSEMANN³ , Samuel EBERT¹, Michael GONSIOR⁴, Janina HAKENMÜLLER⁵, Jakub HALODA⁶, Dennis HARRIES⁷, Dieter HEINLEIN⁸, Harald HIESINGER¹, Rupert HOCHLEITNER⁹, Viktor HOFFMANN¹⁰, Melanie KALIWODA⁹, Matthias LAUBENSTEIN¹¹, Colin MADEN³, Matthias M. MEIER³ , Andreas MORLOK¹, Andreas PACK¹², Alexander RUF^{13,14}, Philippe SCHMITT-KOPPLIN^{13,14}, Maria SCHÖNBÄCHLER³, Robert C. J. STEELE³, Pavel SPURNÝ¹⁵, and Karl WIMMER¹⁶

¹Institut für Planetologie, Westfälische Wilhelms-Universität Münster, Wilhelm-Klemm Str. 10, Münster D-48149, Germany

²Université de Bretagne Occidentale, Institut Universitaire Européen de la Mer, Place Nicolas Copernic, Plouzané Cedex F-29280, France

³ETH Zürich, Institut für Geochemie und Petrologie, Clausiusstrasse 25, Zürich CH-8092, Switzerland

⁴University of Maryland, Center for Environmental Science, Chesapeake Biological Laboratory, 146 Williams Street, Solomons, Maryland 20688, USA

⁵Max-Planck-Institut für Kernphysik, Saupfercheckweg 1, Heidelberg D-69117, Germany

⁶Czech Geological Survey, Geologická 6, Praha 5 CZ-152 00, Czech Republic

⁷Institut für Geowissenschaften, Friedrich-Schiller-Universität Jena, Carl-Zeiss-Promenade 10, Jena D-07745, Germany

⁸German Fireball Network, Lilienstraße 3, Augsburg D-86156, Germany

⁹Mineralogische Staatssammlung München (SNSB), Theresienstr. 41, München D-80333, Germany

¹⁰Department of Geosciences, Eberhard Karls University of Tübingen, Hölderlinstr. 12, Tübingen D-72074, Germany

¹¹Laboratori Nazionali del Gran Sasso, Istituto Nazionale di Fisica Nucleare, Via G. Acitelli 22, Assergi (AQ) I-67100, Italy

¹²Universität Göttingen, Geowissenschaftliches Zentrum, Goldschmidtstr. 1, Göttingen D-37077, Germany

¹³Helmholtz-Zentrum, München, German Research Center for Environmental Health, Analytical BioGeoChemistry, Ingolstädter Landstraße 1, Neuherberg D-85764, Germany

¹⁴Chair of Analytical Food Chemistry, Technische Universität München, Freising-Weihenstephan D-85354, Germany

¹⁵Astronomical Institute of the Czech Academy of Sciences, Fričova 298, Ondřejov CZ-25165, Czech Republic

¹⁶RiesKraterMuseum, Eugene-Shoemaker-Platz 1, Nördlingen D-86720, Germany

*Corresponding author. E-mail: bischoa@uni-muenster.de

(Received 27 September 2016; revision accepted 17 March 2017)

Abstract—On March 6, 2016 at 21:36:51 UT, extended areas of Upper Austria, Bavaria (Germany) and the southwestern part of the Czech Republic were illuminated by a very bright bolide. This bolide was recorded by instruments in the Czech part of the European Fireball Network and it enabled complex and precise description of this event including prediction of the impact area. So far six meteorites totaling 1473 g have been found in the predicted area. The first pieces were recovered on March 12, 2016 on a field close to the village of Stubenberg (Bavaria). Stubenberg is a weakly shocked (S3) fragmental breccia consisting of abundant highly recrystallized rock fragments embedded in a clastic matrix. The texture, the large grain size of plagioclase, and the homogeneous compositions of olivine (Fa_{31.4}) and pyroxene (Fs_{25.4}) clearly indicate that Stubenberg is an LL6 chondrite breccia. This is consistent with the data on O, Ti, and Cr isotopes. Stubenberg does not contain solar wind-implanted noble gases. Data on the bulk chemistry, IR spectroscopy, cosmogenic nuclides, and organic components also indicate similarities to other metamorphosed LL chondrites. Noble gas studies reveal that the meteorite has a cosmic ray exposure (CRE) age of 36 ± 3 Ma and that most of the cosmogenic gases were produced in a meteoroid with a radius of at least 35 cm. This is larger than the size of the meteoroid

which entered the Earth's atmosphere, which is constrained to <20 cm from short-lived radionuclide data. In combination, this might suggest a complex exposure history for Stubenberg.

INTRODUCTION

On Sunday March 6, 2016 at 21:36:51 UT (corresponding to the late local evening, UT+1 h), extended areas of Upper Austria, Bavaria, and the southwestern part of the Czech Republic were illuminated by a very bright fireball. In particular, the inhabitants of Bavaria, where the skies were mostly clear, were stunned by the luminous and sonic effects of the fireball. Observation was difficult in most of Central Europe due to a cloudy sky. Fortunately, parts of western Czech Republic also had partly clear skies in some places and it enabled researchers to obtain the instrumental records provided by the digital autonomous observatories (DAFOs) of the Czech part of the European Fireball Network. These photographic and radiometric records proved to be essential to describe this rare natural event in detail. The cameras at six Czech stations photographed the event at least partly and almost all Czech cameras recorded its light curve by fast photometers with high time resolution of 5000 samples per second. Thanks to these records, the fireball could be described rigorously and with a high reliability and precision (Spurný et al. 2016). Moreover, the impact area of potential meteorites could also be computed and the ground distribution of meteorites could be modeled. This prediction was very precise, because all six recovered meteorites were found almost exactly in the predicted location for the given meteorite masses (Spurný et al. 2016).

In this paper, the mineralogical and chemical characteristics of this new meteorite will be presented including data on organics, short-lived cosmogenic radioisotopes, stable isotopes, and noble gases. The meteorite "Stubenberg" has been accepted by the Nomenclature Committee (*Meteoritical Bulletin Database* 2017) and preliminary data were published by Ebert and Bischoff (2016) and Spurný et al. (2016). After the meteorite falls of Braunschweig (L6; Bartoschewitz et al. 2017), Žďár nad Sázavou (Spurný 2016; Spurný et al. 2016), and Ejby (H5/6; *Meteoritical Bulletin Database* 2017; Spurný et al. 2017), Stubenberg is the fourth recovered meteorite fall within less than 3 yr impacting Earth only ~800 km apart. Less than 10 meteorite falls/year are recovered globally, and hence, this concentration of recorded falls is remarkable.

SAMPLES AND METHODS—SUMMARY

In order to obtain information about the classification of the rock and to reveal details on chemical, physical, and mineralogical features and characteristics of the rock different analytical methods were applied. This is a brief summary and further details are given in Data S1 in supporting information. Several thin and thick sections and fragments of Stubenberg were studied using optical and electron microscopy. Electron microscopic studies with various scanning and transmission electron microscopes (SEM, TEM) were performed in Münster, Jena, Prague, and Munich and chemical data by electron microprobe were obtained in Münster. Raman spectroscopical investigations (Munich) were conducted with a Horiba Xplora integrated confocal laser micro Raman system on an Olympus BX51 microscope.

After homogenizing 0.5 g of interior material, a 200 mg whole-rock sample of fragments and splinters was analyzed for major and trace element concentrations by inductively coupled plasma atomic emission spectroscopy (ICP-AES) and inductively coupled plasma sector field mass spectrometry (ICP-SFMS) following the procedure described by Barrat et al. (2012, 2015, 2016). Cosmogenic radionuclide concentrations were analyzed by means of nondestructive high purity germanium (HPGe) gamma spectroscopy in the underground laboratories at the Laboratori Nazionali del Gran Sasso and at the Max-Planck-Institut für Kernphysik in Heidelberg (Arpesella 1996; Heusser et al. 2015), and bulk oxygen isotope composition was analyzed by laser fluorination in combination with gas source mass spectrometry (Sharp 1990). The data were normalized to the composition of San Carlos olivine ($\delta^{17}\text{O}_{\text{VSMOW2}} = 2.715 \text{ ‰}$, $\delta^{18}\text{O}_{\text{VSMOW2}} = 5.220 \text{ ‰}$; see Pack et al. 2016).

For the Ti-Cr isotope analyses sample powders of Stubenberg ($2 \times 50 \text{ mg}$) were dissolved and purified using ion exchange chromatographic procedures. Titanium isotope analyses were then carried out using a Thermo Fisher Scientific Neptune Plus multicollector-inductively coupled plasma mass spectrometer (MC-ICPMS) both at the Institut für Planetologie in Münster and at the Institute of Geochemistry and Petrology at ETH Zurich, while Cr isotopes were analyzed in Zurich

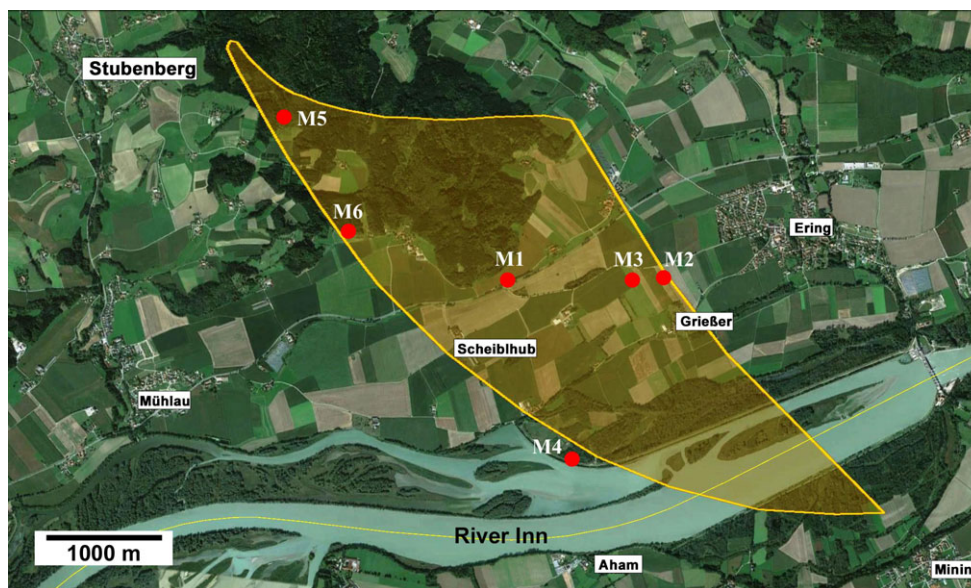


Fig. 1. Calculated strewn field near Stubenberg (Germany) with find locations of the six recovered individuals (M1–M6). The northern part of the strewn field is dominated by forest, in which the samples M5 and M6 were found. Most other areas represent farmland. The river “Inn” marks the border to Austria in the south. Source of base map: Google Earth.

only. The analytical procedures followed those described in Schönbachler et al. (2004), Williams (2015), and Zhang et al. (2011) for Ti and in Steele and Schönbachler (2016) for Cr and are described in more detail in Data S1. The noble gases He-Xe present in two bulk samples “I” (23.3 mg) and “II” (71.5 mg) were analyzed at ETH Zurich using the standard procedures described in detail by Riebe et al. (Forthcoming).

Regarding physical properties, Fourier transform infrared spectroscopy (FTIR) spectroscopic measurements were undertaken using a Bruker Vertex 70v at the IR/IS laboratory located at the Institut für Planetologie (Münster) and the Magnetic Susceptibility (MS) of various Stubenberg fragments was measured in the strewn field as well as in Nördlingen with the SM30 of ZH Instruments. Additional instrumental details are given in Data S1. A destructive methanolic solvent extraction of organic matter was performed in an agate mortar using 50 mg of freshly broken fragments of the Stubenberg meteorite. Analytical details and information on the data processing are given in Schmitt-Kopplin et al. (2010, 2012), Tziotis et al. (2011), Hertkorn et al. (2015), and Ruf et al. (2017).

RESULTS

Fall Circumstances and Geographic Details of Find Area

From the detailed light curve of the observed bolide taken by the fast photometers (time resolution 5000 samples/s) as part of the Czech fireball automated

cameras (Spurný et al. 2007), it was evident that the initial meteoroid was heavily fragmented in the last third of its luminous atmospheric flight. A very complex model of the impact area was produced using precise trajectory data combined with the known wind profile available from balloon data. The distribution pattern of individual meteorites deposited from each particular breakup was directly visible on the light curve, which will be described along with the bolide data elsewhere. The resulting predicted impact area near the village of Stubenberg in Lower Bavaria has a complicated irregular shape (Fig. 1). This prediction was convincingly confirmed by the positions and masses of the recovered meteorites, as described in Fig. 1. The northern part of the strewn field is dominated by forest at an elevation of about 500 m above sea level, in which the samples M5 and M6 were found (Table 1). Most other areas represent farmland (Fig. 1). Stubenberg is a small village in Lower Bavaria with a population of about 1400 residents.

Petrography and Mineralogy

Description of Hand Specimens

All recovered stones of the Stubenberg meteorite are shown in Fig. 2 and listed in Table 1. The first fragments of one broken individual stone were found 6 days after the fall. Within several weeks of intensive search six meteorite individuals with a total mass of 1473 g were recovered. The largest fragment (M5) has a mass of 1320 g (Figs. 1 and 2e; Table 1), and a bulk

Table 1. The Stubenberg meteorite finds (GPS coordinates of the locations referring to the WGS84 datum). The polished sections studied in Münster and Jena were prepared from the 1.298 g piece of M1d and M6, respectively. The bulk chemical studies (Brest) and isotopic studies (Zurich) were performed on samples of M1h.

No.	Mass (g)	Date of find (yyyy/mm/dd)	Latitude (N) Longitude (E)	Characteristics of the meteorite piece; Finder of the specimen
M1	47.88	2016/03/12	48° 17' 42.9" 13° 06' 58.9"	Meteorite was scattered into 17 pieces at the impact (M1a–M1n); Michael Krippner: 6.21 g (M1a), Sabine Gumpenberger: 23.58 g (M1b), Mathias Stricker: 5.42 g (M1e), and seven other finders
M2	7.66	2016/03/23	48° 17' 44.9" 13° 07' 57.7"	Individual meteorite, broken into two (fitting) parts of 7.21 g (M2a) and 0.45 g (M2b) at the impact; Ralph Sporn + Martin Neuhofer
M3	19.24	2016/03/23	48° 17' 43.9" 13° 07' 45.8"	Meteorite fragment with primary and secondary fusion crust; Ralph Sporn + Martin Neuhofer
M4	42.43	2016/03/26	48° 16' 58.5" 13° 07' 25.0"	Complete individual meteorite with signs of flight orientation; Moritz Karl
M5	1320	2016/04/01	48° 18' 20.9" 13° 05' 36.5"	Complete, flight oriented individual meteorite with deep regmaglypts; Ralph Sporn + Martin Neuhofer
M6	35.89	2016/04/03	48° 17' 53.6" 13° 05' 59.9"	Meteorite fragment with fusion crust and broken faces; Dennis Harries
Total	1473		48° 17.7' 13° 07.0'	

density of $3.29 \pm 0.01 \text{ g cm}^{-3}$. The first recovered piece was heavily fragmented at the impact location, when hitting the ground. The main mass broke into three larger pieces and several smaller fragments (M1a–M1n; Table 1) covering an area of $\sim 10 \text{ m}$ in diameter. From the time of impact until recovery the fragmented piece remained in place. The biggest fragment M1b has a weight of 23.58 g (Fig. 2a); all pieces are 0.1–0.3 mm thick, dark-brown to black and fusion crust is mostly well preserved. While the surface of the meteorite is predominantly smooth, the fusion crust shows polygonal cracks in several spots. Meteorite piece M6, weighing 35.89 g (Fig. 2f), was found as a fragmented individual with two almost perpendicular fracture surfaces not covered by fusion crust. Intensive search did not yield the missing fragments. Close inspection by SEM later showed abundant FeS melt splashes and rare glass droplets on the broken surfaces, suggesting a high altitude breakup event, possibly at the end or slightly after the luminous flight. Cutting the meteorite by a wire saw revealed a rather friable rock.

Internally, a grayish, silicate-rich component dominates the meteorite; rare millimeter-sized fragments are visible; and minor amounts of minerals with metallic luster are recognizable throughout the rock. Rarely, shock veins are observed consisting of the metallic phases and troilite as confirmed by detailed mineralogical studies on thin sections. Since the rock was found about 1 week after the fall, it had already been affected by some minor weathering processes as documented in places by the brownish taint on the surfaces of the broken piece.

Mineralogy—Texture and Compositions of Phases

The brecciated meteorite has abundant fragments with a recrystallized texture and a small number of chondrule relics (Fig. 3). Especially, the outlines of former barred-olivine (BO) and radial pyroxene (RP) chondrules are still recognizable (Fig. 3). One of these relic chondrules is a several millimeter-sized macrochondrule (Weyrauch and Bischoff 2012). The distribution and obtained abundances of various phases are shown in Fig. S1 and listed in Table S1 in supporting information.

Olivine is by far the most abundant phase (53–56 vol%; Table S1). Generally, the grains are variable in size and show strong undulatory extinction. The olivines are homogeneous in composition throughout all thin sections. The mean composition of 54 analyzed olivines is $\text{Fa}_{31.4 \pm 0.3}$ with a compositional range between 30.5 and 32.2 mol% Fa (Table 2). The low-Ca pyroxenes ($\sim 17 \text{ vol\%}$) and Ca-pyroxenes (6.3 vol%) have mean compositions of $\text{Fs}_{25.4}\text{Wo}_{2.0}$ and $\text{Fs}_{10.3}\text{Wo}_{43.9}$, respectively (Table 2; Fig. S1). The 43 analyzed low-Ca pyroxenes vary between 24.8 and 26.1 mol% Fs. Ca-pyroxene has a much lower modal abundance compared with low-Ca pyroxene and is also homogeneous in composition. Raman mapping supports that the dominating phases of Stubenberg are olivine, orthopyroxene, Ca pyroxene, and Ab-rich plagioclase. According to the Raman spectra, all pyroxenes show very uniform compositions with insignificant variations not only in one single clast but also from clast to clast. Selected olivine and pyroxene particles have been tested for water ($\text{H}_2\text{O}/\text{OH}$) content by Raman spectroscopy,

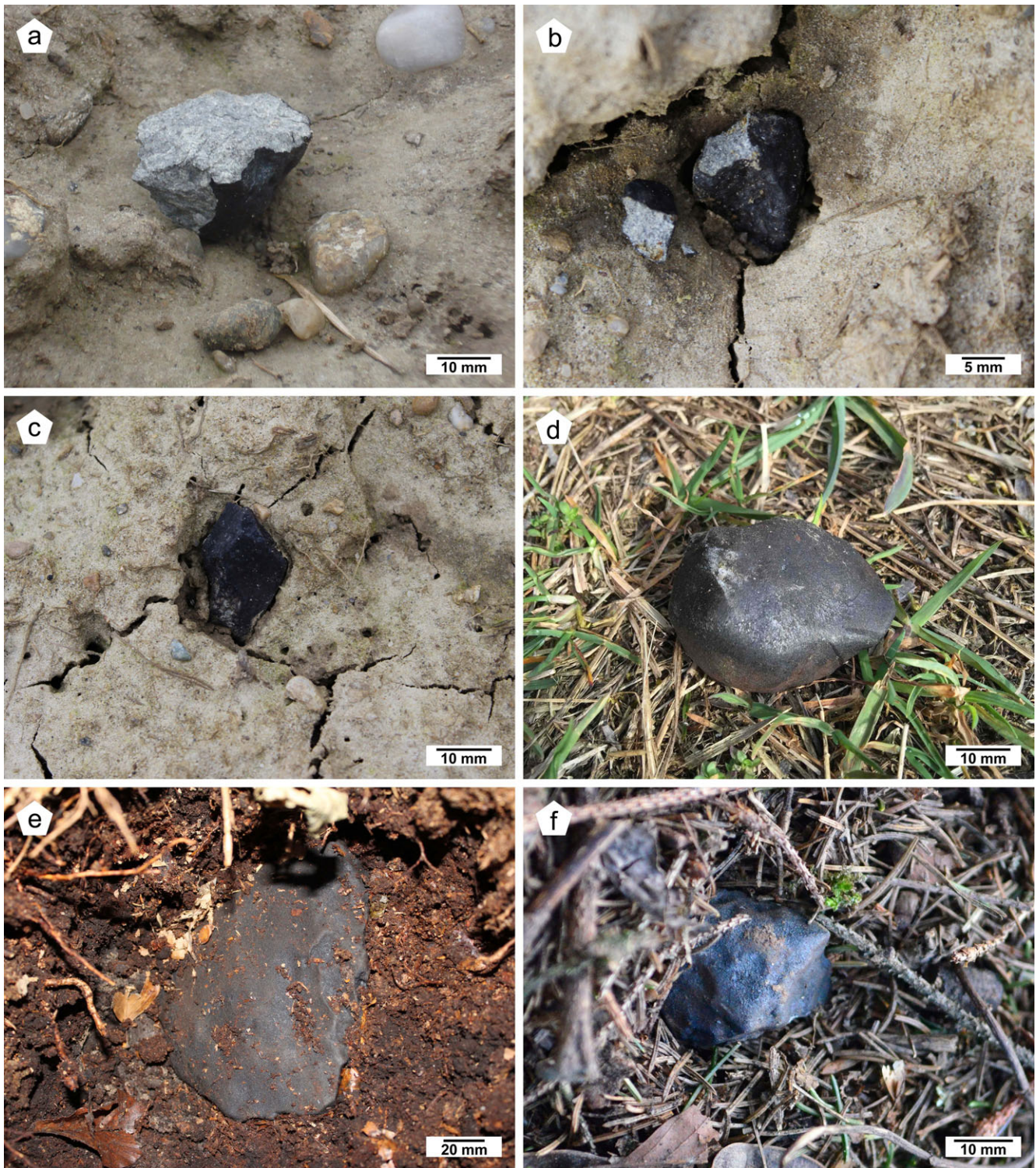


Fig. 2. Images of the six Stubenberg meteorites found between March 12 and April 3, 2016. a) This broken fragment, M1b, of 23.58 g is the largest part of 17 pieces, totaling 47.88 g. b) A chip of 0.45 g broke off from the individual meteorite M2 of 7.66 g at the impact in a field. c) The meteorite fragment M3 weighing 19.24 g was partially buried in the soft ground. d) Complete individual meteorite M4 of 42.43 g found on the northern bank of the river Inn. e) The impact hole of the largest Stubenberg individual meteorite M5 of 1320 g in the forest ground was 14 cm deep. f) The fragment M6 weighing 35.89 g shows fusion crust on the top, and broken faces at the bottom.

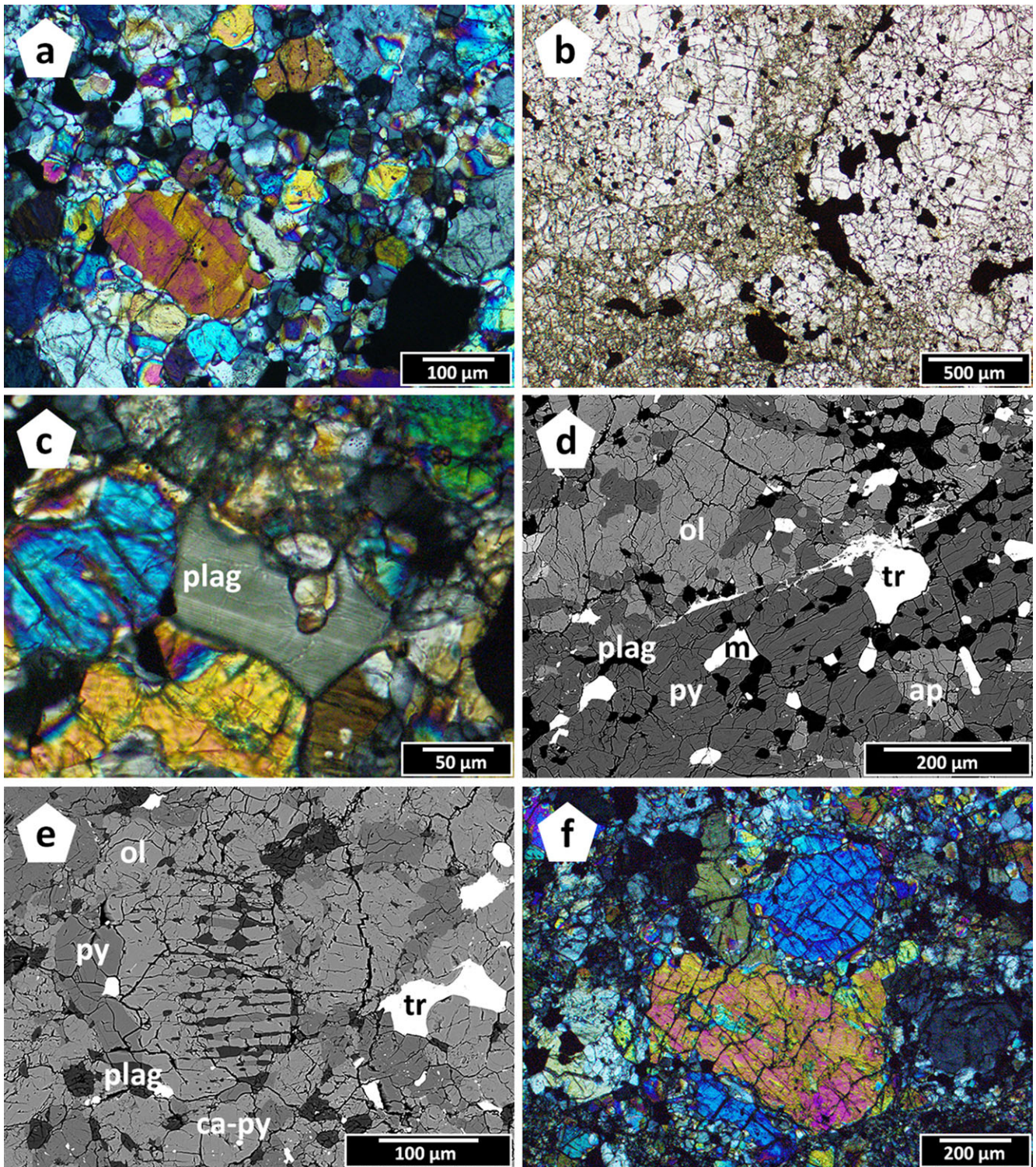


Fig. 3. Photomicrographs of typical features of the Stubenberg fragmental breccia. a) Highly recrystallized texture within an LL6 fragment. b) Fragmented appearance of the bulk rock. The boundaries of individual fragments are well observable. c) Large plagioclase grains are common as well as thin shock veins shown in (d). e) Occasionally, relict chondrules like this BO-chondrule are visible. f) Olivines show several sets of planar fractures. Abbreviations: plag = plagioclase, ol = olivine, py = low-Ca pyroxene, ap = apatite, m = metal, tr = troilite, ca-py = Ca-pyroxene. Images in polarized light (a, b, c, f), crossed Nicols (a, c), images in backscattered electrons (d, e).

Table 2. Chemical composition of main phases in the Stubenberg fragmental breccia. All data in wt% and obtained by electron microprobe.

wt%	Olivine	Pyroxene	Ca-Pyroxene	Plagioclase	Apatite	Merrillite	Chromite
	<i>n</i> = 54	<i>n</i> = 43	<i>n</i> = 6	<i>n</i> = 42	<i>n</i> = 16	<i>n</i> = 4	<i>n</i> = 14
SiO ₂	36.8	54.3	53.4	65.3	0.19	0.18	<0.03
TiO ₂	<0.02	0.20	0.46	0.05	<0.02	<0.01	3.4
Al ₂ O ₃	<0.01	0.16	0.47	20.9	<0.01	<0.01	5.2
Cr ₂ O ₃	<0.02	0.15	0.81	<0.01	<0.01	<0.01	54.5
FeO	27.8	16.5	6.4	0.53	0.59	0.62	32.7
MnO	0.47	0.46	0.22	<0.01	<0.02	n.d.	0.64
MgO	34.0	26.4	16.0	<0.03	0.15	3.4	1.51
CaO	<0.01	1.01	21.3	2.20	52.3	46.1	n.d.
Na ₂ O	<0.01	<0.03	0.52	9.1	0.33	2.43	<0.01
K ₂ O	<0.01	<0.01	n.d.	0.92	<0.01	0.08	<0.01
P ₂ O ₅	<0.04	<0.01	<0.01	<0.02	39.6	46.4	<0.01
Cl	<0.01	<0.01	n.d.	n.d.	5.7	0.48	<0.01
Total	99.1	99.2	99.6	99.0	98.9	99.7	98.0
Fa	31.4 ± 0.3						
Fs		25.4 ± 0.3	10.3 ± 0.4				
Wo		2.0 ± 0.3	43.9 ± 0.4				
An				11.1 ± 0.4			
Or				5.5 ± 1.2			

n.d. = not detected; *n* = number of analyses.

but no Raman signals could be detected in the H₂O Raman spectral region (3400–3700 cm⁻¹) due to possible rapid terrestrial weathering of the mineral constituents at the impact location.

Plagioclase (10–13 vol%; Table S2 in supporting information) is present as quite large crystals often exceeding 100 μm in size (Fig. 3). Mean plagioclase has An and Or components of 11.1 ± 0.4 and 5.5 ± 1.2 mol %, respectively (*n* = 42; Table 2). The compositions vary between 10.3 and 12.1 mol% An. Both the phosphates merrillite and Cl-apatite were found in the studied thin sections. Cl-apatite is more abundant than merrillite. Their compositions are listed in Table 2.

Metal and sulfide occur as small grains distributed throughout the entire thin sections. Metallic phases are homogeneously distributed and up to 250 μm in apparent size. The chemical compositions of these phases are given in Table S2. In general, kamacite has mean Ni and Co concentrations of 3.9 and 6.1 wt%, respectively. The taenite composition is variable, with Ni content varying from 41.9 to 48.2 wt% (average ~44.3 wt% Ni, ~1.8 wt% Co, 0.22 wt% Cu; *n* = 38). Some grains may be tetrataenite due to slight anisotropy in reflected, polarized light.

Troilite is an abundant phase in Stubenberg (approx. 9 vol%; Table S1) and is distributed throughout all thin sections, occasionally forming millimeter-sized aggregates. An approximately 1.5 mm long, string-shaped aggregate of troilite and Ni-poor pentlandite (molar Fe/Ni ~3.3; Table S2) was observed (Fig. 4). Small amounts of

pentlandite also occur in association with other troilite grains. Pentlandite was confirmed by TEM using selected area electron diffraction (SAED) obtained on a FIB section (Fig. 4c). At the TEM scale the pentlandite shows strong mosaicism, that is, poor crystal quality, and sharp boundaries to neighboring troilite. {111} and {0-11} of pentlandite are nearly parallel with (001) and {010} of troilite, respectively (Fig. 4d). This is close to the orientation relationship observed for troilite/pyrrhotite and exsolved pentlandite in terrestrial and meteoritic samples (Harries and Langenhorst 2013). The coexisting troilite shows good crystal quality and contains abundant subgrain boundaries. Superstructure reflections of pyrrhotite are absent in SAED patterns, indicating nearly stoichiometric FeS.

Chromite occurs as small grains and has mean MgO, Al₂O₃, and TiO₂ concentrations of 1.5 wt%, 5.2 wt%, and 3.4 wt%, respectively (*n* = 14; Table 2). Chromite has been frequently found in all fragments. It shows anhedral grains up to 100 μm and is, according to its Raman spectrum, a high iron, low magnesium member of the solid solution. Rarely do some grains show deviating peak positions, which point to possibly higher concentrations of Mg and/or Al.

Additional accessory phases observed are ilmenite with grain sizes up to 50 μm (associated with taenite and troilite, or with chromite), metallic copper (grains <10 μm, associated with kamacite, taenite), rutile, anatase, and carbon phases (graphite to heavily disordered graphite). The latter three phases were

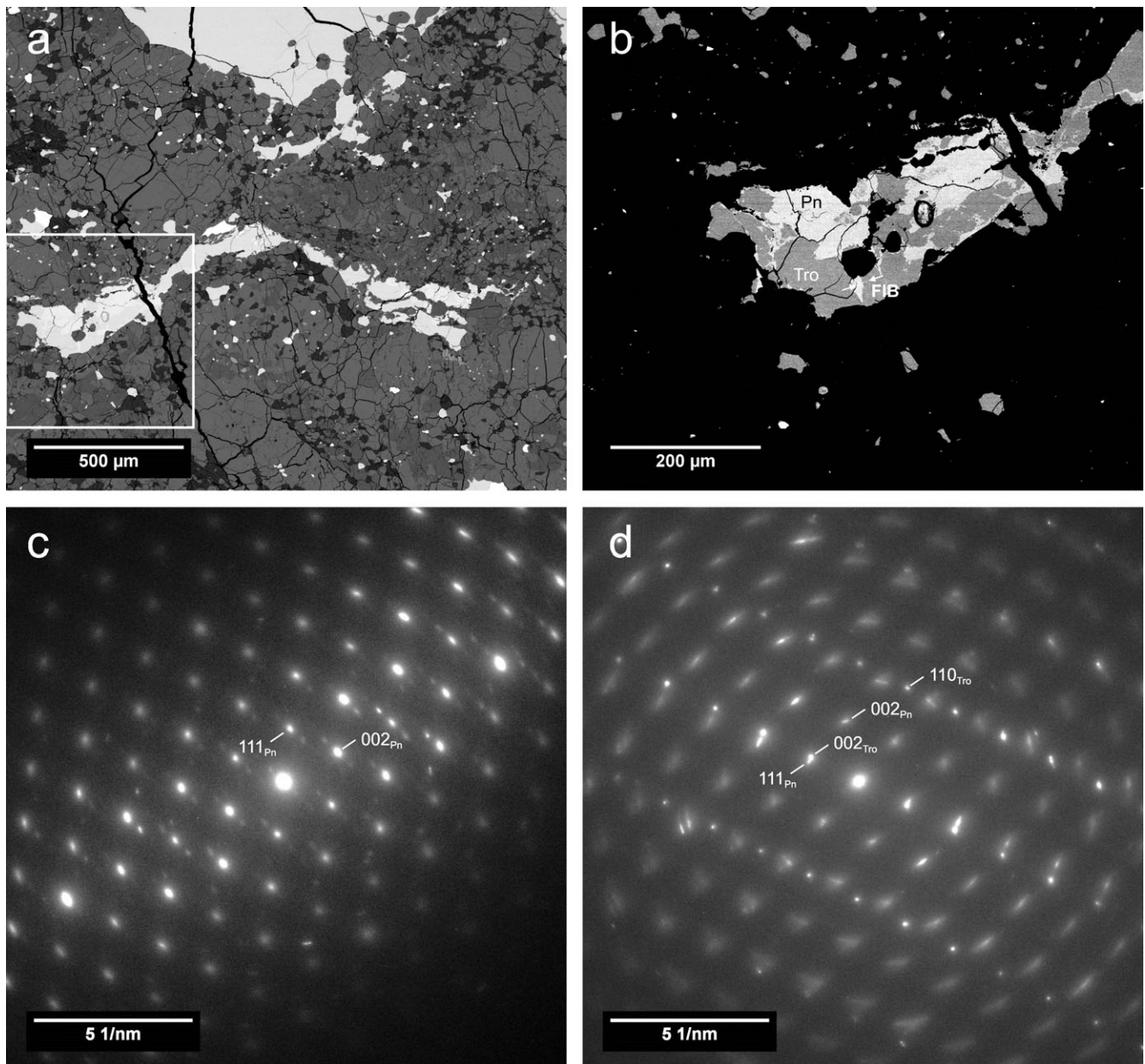


Fig. 4. Pentlandite in the Stubenberg meteorite. a) SEM-BSE overview showing the elongated pentlandite-troilite aggregate. b) SEM-BSE detail showing the intergrowth of pentlandite (Pn) and troilite (Tro). Arrows mark the location of an extracted FIB section. c) TEM-SAED pattern of pentlandite close to zone axis [1–10]. d) TEM-SAED pattern of pentlandite and troilite showing the orientation relationship outlined in the text.

identified by Raman spectroscopy. The two different TiO_2 phases, anatase and rutile, could be clearly identified as single grains by their different Raman spectra (Fig. S2 in supporting information). Rutile displays white to colorless grains up to 20 μm . Both phases are found in direct contact with ilmenite and chromite. Carbon phases have mainly been detected decorating grain boundaries between silicate and sulfide grains. According to the band width of the main Raman

bands they vary between well-crystallized graphite and heavily disordered phases. As all measurements have been conducted on simply broken surfaces, the disorder cannot be an artifact due to mechanical treatment, and contamination by grinding or coating can be excluded. On the broken surface large grains of olivine, pyroxene, feldspar, and troilite are often recognizable as well as 120° triple junctions between olivine, pyroxene, and plagioclase (Fig. 5).

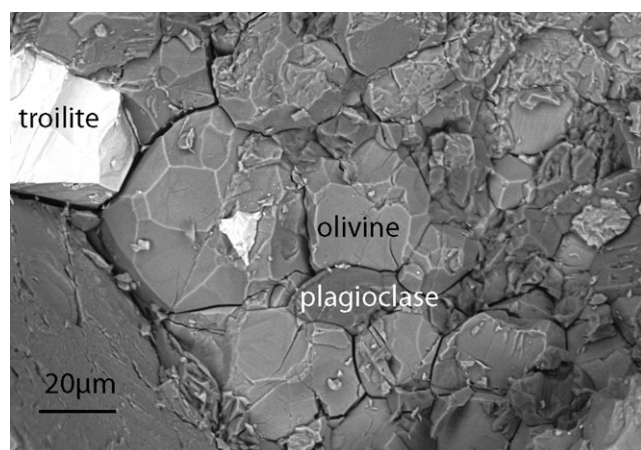


Fig. 5. BSE image of the broken surface of fragment M1h (1.652 g) of the Stubenberg meteorite with troilite (white) and abundant olivine (light gray). The dark gray grains represent plagioclase. Note the well-preserved 120° triple junctions between the mineral phases.

Shock Metamorphism and Weathering

As stated above, based on the study of the thin sections Stubenberg is brecciated (Fig. 3b). The thin sections only show highly recrystallized fragments having only very rare relic chondrules (type 6). Several shock veins were observed (Fig. 3d). Plagioclase and olivine show undulatory extinction, and the olivines show distinct sets of planar fractures (Fig. 3f). High-pressure phases (such as ringwoodite) were searched for by Raman spectroscopy, but could not be detected even in the melt veins. No glass-like or recrystallized plagioclase phases could be found (including feldspar glasses or maskelynite). The optical features indicate that the rock is weakly shocked (S3; Stöffler et al. 1991; Bischoff and Stöffler 1992).

The residence time of about 7 days on the ground resulted in the first signs of weathering. Locally, areas with a brownish taint are already present resulting from the first breakdown of metals. Although a few rusty spots are clearly recognized with the naked eye on the surface of all samples, alteration phases such as iron oxides–hydroxides or iddingsite (olivine alteration) could not be detected by Raman spectroscopy.

Chemical Characteristics

Bulk Chemistry

A number of small interior fragments of about 0.5 g free of fusion crust were provided for chemical characterization. The results summarized in Table 3 and shown in Fig. 6 indicate that the chemical composition of Stubenberg is close to the composition of Chelyabinsk (Righter et al. 2015) and that the Stubenberg chondrite is not chemically anomalous.

Table 3. The bulk composition of Stubenberg. Oxides in wt%, all other elements in ppm.

wt%	ICP-AES	ICP-SFMS	ppm	ICP-SFMS
TiO ₂	0.13	0.12	Zr	5.12
Al ₂ O ₃	2.17		Nb	0.419
Fe ₂ O ₃	29.8		Cs	0.0389
MnO	0.36	0.34	Ba	3.6
MgO	24.9		La	0.451
CaO	1.82	1.90	Ce	1.17
Na ₂ O	0.98		Pr	0.175
K ₂ O	0.1	0.11	Nd	0.858
P ₂ O ₅	0.31	0.30	Sm	0.272
ppm			Eu	0.0825
Cr	4573		Gd	0.387
Li		2.29	Tb	0.0693
Be		0.0287	Dy	0.46
K		950	Ho	0.101
Sc	8.7	9.33	Er	0.294
V	89	80.6	Tm	0.0437
Mn		2606	Yb	0.274
Co	578	536	Lu	0.0405
Ni	12262		Hf	0.144
Cu		73.1	Ta	0.0193
Zn		43.54	W	0.121
Ga		5.06	Pb	0.102
Rb		2.88	Th	0.0476
Sr	12	10.88	U	0.0063
Y	2.8	2.97		

Noble Gases

Noble gas results for the two interior fragments of Stubenberg sample M1h (described here as Stubenberg I and II) are summarized in Tables 4–6. All noble gases can be explained with a mixture of cosmogenic, radiogenic, and a very small amount of heavy (Ar–Xe) trapped noble gases. Most importantly, Stubenberg does not contain solar wind noble gases (Fig. 7), because of the low ⁴He and ²⁰Ne concentrations that are entirely of cosmogenic (cos) and radiogenic (rad) origin, the lack of trapped ²⁰Ne, and the very small concentration of trapped (tr) ³⁶Ar (Table 7). Hence, Stubenberg cannot be a regolith breccia.

The heavier noble gases are all meteoritic, as shown with the (low) heavy element ratios ³⁶Ar_{tr}/¹³²Xe (= 20 and 38, respectively) and ⁸⁴Kr/¹³²Xe (= 0.78 and 0.74), and the high ⁴⁰Ar/³⁶Ar (= 3900 and 4100) and ¹²⁹Xe/¹³²Xe (= 1.90 and 1.95) ratios.

We used the depth- and chemistry-dependent model by Leya and Masarik (2009) to determine the cosmic ray exposure (CRE) age of Stubenberg, assuming a simple “4π” irradiation in space and taking into account the bulk chemistry for Stubenberg given in this work (Table 3). Using the LL chemistry that is given in the Leya and Masarik (2009) data tables yields the same

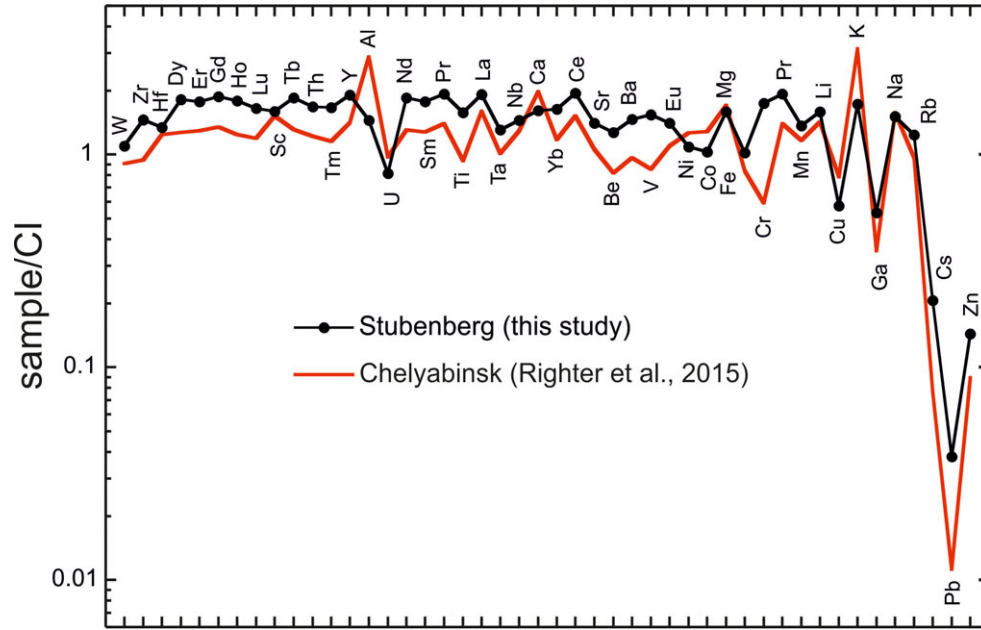


Fig. 6. Bulk composition of Stubenberg in comparison to the LL chondrite Chelyabinsk. Chelyabinsk data from Richter et al. (2015). For normalization the CI-values of Barrat et al. (2012) are used.

Table 4. Noble gas concentrations and isotope ratios in Stubenberg: He, Ne, and Ar.

	Mass/mg	^4He	$^3\text{He}/^4\text{He}$	^{20}Ne	$^{20}\text{Ne}/^{22}\text{Ne}$	$^{21}\text{Ne}/^{22}\text{Ne}$	^{36}Ar	$^{38}\text{Ar}/^{36}\text{Ar}$	$^{40}\text{Ar}/^{36}\text{Ar}$
I	23.31 ± 0.01	1184.7 ± 1.2	618 ± 6	14.53 ± 0.06	0.8361 ± 0.0027	0.9237 ± 0.0023	1.46 ± 0.05	1.37 ± 0.04	3890 ± 140
II	71.48 ± 0.01	1201.6 ± 2.7	602 ± 5	14.11 ± 0.10	0.87 ± 0.04	0.95 ± 0.04	1.36 ± 0.05	1.19 ± 0.06	4060 ± 160

He, Ne, Ar concentrations in $10^{-8} \text{ cm}^3 \text{ g}^{-1} \text{ STP}$.

results. We did not renormalize the radii according to density. All radii in the Leya and Masarik (2009) work are given for meteoroids with a density of 3.50 g cm^{-3} . The typical LL meteorite density might be 3.29 g cm^{-3} (Wilkison and Robinson 2000), which would increase all radii by 6%. However, we do not exactly know the bulk density of the Stubenberg meteoroid, that is, we cannot take into account possible macroporosity.

The measured ^3He and ^{21}Ne concentrations are entirely cosmogenic, the ^{38}Ar is corrected for 2 and 4% trapped ^{38}Ar , respectively (see Table 7 for details). As Ne is entirely cosmogenic, the measured $^{22}\text{Ne}/^{21}\text{Ne}$ ratio can be used directly as a shielding indicator. The precisely measured $^{22}\text{Ne}/^{21}\text{Ne}$ ratio in Stubenberg I of 1.0826 ± 0.0026 suggests a preatmospheric radius of $\geq 35 \text{ cm}$. The preatmospheric mass of 600 kg, based on fireball observations (Spurný et al. 2016), yields the same radius of 35 cm. A higher mass within a conservative factor of two (1200 kg; radius of $\sim 45 \text{ cm}$) would still be consistent with the noble gas data. However, these radii are incompatible with short-lived radionuclide data, which suggest a smaller radius. As discussed later, both data sets can be brought into agreement, if the Stubenberg meteoroid experienced a

recent collision which decreased its radius. In the Leya and Masarik model, we hence average the cosmogenic ^3He , ^{21}Ne , and ^{38}Ar production rates for all “allowed” sample depths for meteoroids with 35–50 cm radius, that is, where the predicted $^{22}\text{Ne}/^{21}\text{Ne}$ matches the measured one within uncertainty. The most likely shielding depth would then be 10–12 cm for the samples analyzed here (Leya and Masarik 2009). The “uncertainty” of the resulting production rates given in Table 7 covers the maximum and minimum values obtained for all allowed conditions. Note that systematic uncertainties of the Leya and Masarik (2009) production rate model, assumed to be $\sim 15\text{--}20\%$ are not included in the uncertainties given in Table 8.

Data points of both samples plot close to or above the “Bern line” in $^3\text{He}/^{21}\text{Ne}$ versus $^{22}\text{Ne}/^{21}\text{Ne}$ space (see, for example, fig. 5 of Scherer et al. 1998) suggesting that Stubenberg did not lose cosmogenic ^3He during its travel to Earth.

Radionuclides

The activities for the very short-lived radionuclides are given in Table 9 and the naturally occurring radionuclides (Table S3 in supporting information) are

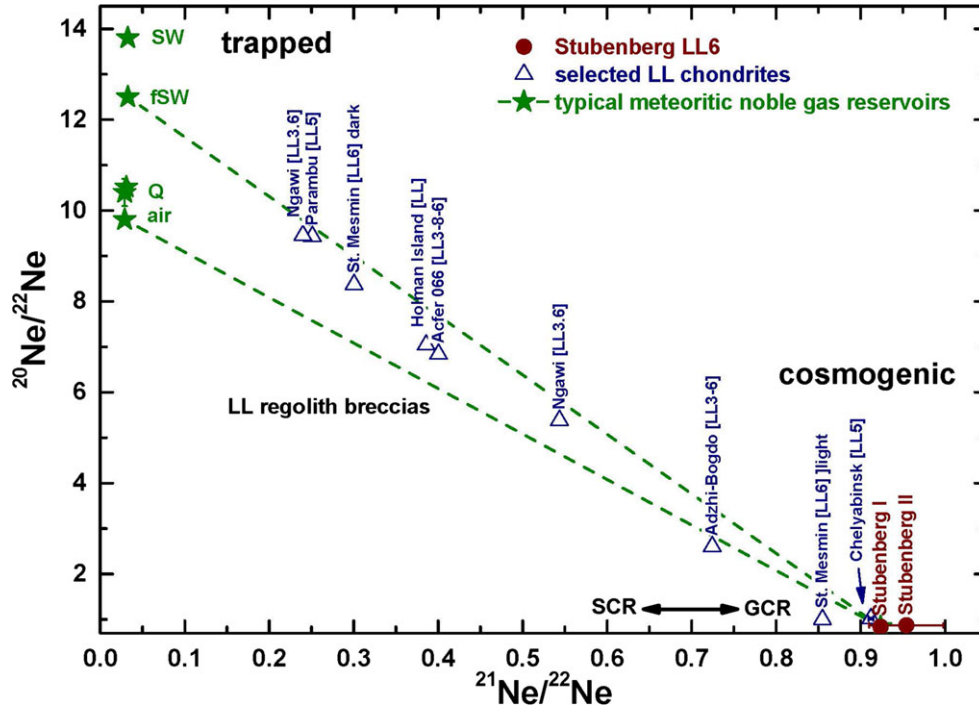


Fig. 7. Neon isotopes show that Stubenberg does not contain implanted solar wind noble gases. Both data points plot exactly on the cosmogenic endmember composition, implying that contributions from trapped Ne are negligible. For comparison, data for a selection of LL chondrites that contain mostly trapped Ne (in most cases fractionated solar wind [fSW], are also shown. Typical pure trapped Ne endmembers (air, SW [Heber et al. 2009], and Q [Busemann et al. 2000, 2014] plot in the upper left of the figure). References for LL chondrite literature data: Heymann and Mazor (1966); Bischoff et al. (1993); Eugster et al. (1993); Scherer et al. (1998); Schultz and Franke (2004).

Table 5. Noble gas concentrations and isotope ratios in Stubenberg: Kr and Xe.

	^{84}Kr	$^{78}\text{Kr}/^{84}\text{Kr}$	$^{80}\text{Kr}/^{84}\text{Kr}$	$^{84}\text{Kr} = 100$ $^{82}\text{Kr}/^{84}\text{Kr}$	$^{83}\text{Kr}/^{84}\text{Kr}$	$^{86}\text{Kr}/^{84}\text{Kr}$	$^{124}\text{Xe}/^{132}\text{Xe}$	$^{126}\text{Xe}/^{132}\text{Xe}$
I	0.733 ± 0.027	1.68 ± 0.07	15.0 ± 0.5	27.7 ± 1.0	28.0 ± 0.9	28.9 ± 1.2	0.73 ± 0.03	0.78 ± 0.06
II	0.668 ± 0.019	1.88 ± 0.03	14.71 ± 0.17	28.1 ± 0.5	27.6 ± 0.6	28.8 ± 0.4	0.705 ± 0.025	0.821 ± 0.024

Kr concentration given in $10^{-10} \text{ cm}^3 \text{ g}^{-1} \text{ STP}$.

Table 6. Noble gas concentrations and isotope ratios in Stubenberg: Xe continued.

	^{132}Xe	$^{128}\text{Xe}/^{132}\text{Xe}$	$^{129}\text{Xe}/^{132}\text{Xe}$	$^{132}\text{Xe} = 100$ $^{130}\text{Xe}/^{132}\text{Xe}$	$^{131}\text{Xe}/^{132}\text{Xe}$	$^{134}\text{Xe}/^{132}\text{Xe}$	$^{136}\text{Xe}/^{132}\text{Xe}$
I	0.95 ± 0.04	8.9 ± 0.4	190 ± 8	15.7 ± 0.9	80 ± 4	38.5 ± 1.8	32.9 ± 1.5
II	0.904 ± 0.024	9.04 ± 0.19	195 ± 3	16.2 ± 0.3	81.3 ± 1.5	39.2 ± 0.7	32.9 ± 0.6

Xe concentration given in $10^{-10} \text{ cm}^3 \text{ g}^{-1} \text{ STP}$.

in agreement with the average concentrations in ordinary LL chondrites (Wasson and Kallemeyn 1988).

Oxygen Isotopes

The oxygen isotope composition of the analyzed fragment of Stubenberg is $\delta^{17}\text{O} = 3.854 \text{ ‰}$ and $\delta^{18}\text{O} = 5.067 \text{ ‰}$ (Figs. S3 in supporting information and 8). This gives an offset in $\delta^{17}\text{O}$ of $\Delta,^{17}\text{O} = 1.216 \text{ ‰}$

relative to a reference line with a slope of 0.5305 that passes through San Carlos olivine ($\Delta,^{17}\text{O} = 0 \text{ ‰}$). The data for Stubenberg are consistent with those of other LL chondrites.

Titanium Isotopes

The Ti isotope compositions of Stubenberg measured in Münster ($n = 12$; $\varepsilon^{46}\text{Ti} = -0.08 \pm 0.11$, $\varepsilon^{48}\text{Ti} =$

Table 7. Radiogenic, trapped, and cosmogenic noble gas concentrations and production rates used.

	${}^4\text{He}_{\text{rad}}^{\text{a}}$	${}^{40}\text{Ar}_{\text{rad}}^{\text{a}}$	${}^{36}\text{Ar}_{\text{tr}}^{\text{a}}$	${}^3\text{He}_{\text{cos}}^{\text{a}}$	${}^{21}\text{Ne}_{\text{cos}}^{\text{a}}$	${}^{38}\text{Ar}_{\text{cos}}^{\text{a}}$	P_3^{b}	P_{21}^{b}	P_{38}^{b}
I	771 ± 33	5690 ± 280	0.18 ± 0.07	73.2 ± 0.7	15.8 ± 0.4	1.966 ± 0.008	1.957	0.4227	0.0501
II	793 ± 33	5530 ± 310	0.35 ± 0.06	72.3 ± 0.6	15.5 ± 0.3	1.562 ± 0.007	± 0.036	± 0.008	± 0.0011

^a ${}^4\text{He}_{\text{cos}}$ subtracted with $({}^4\text{He}/{}^3\text{He})_{\text{cos}} = 5.65 \pm 0.45$ (Wieler 2002), ${}^3\text{He}_{\text{measured}} = {}^3\text{He}_{\text{cos}}$ and ${}^{21}\text{Ne}_{\text{measured}} = {}^{21}\text{Ne}_{\text{cos}}$. ${}^{38}\text{Ar}_{\text{cos}}$ is obtained by decomposition of the measured ${}^{36}\text{Ar}/{}^{38}\text{Ar}$ into trapped (${}^{36}\text{Ar}/{}^{38}\text{Ar} = 5.32\text{--}5.34$, air or Q; Busemann et al. 2000) or cosmogenic (${}^{36}\text{Ar}/{}^{38}\text{Ar} = 0.63\text{--}0.67$). The variations are covered in the uncertainty of ${}^{38}\text{Ar}_{\text{cos}}$. The measured ${}^{40}\text{Ar}$ is assumed to be entirely radiogenic. At maximum 0.9 and 1.8%, respectively, of the ${}^{40}\text{Ar}$ in I and II could be atmospheric, assuming ${}^{36}\text{Ar}_{\text{tr}}$ to be entirely air.

^bProduction rates were determined based on the most precise shielding indicator, ${}^{22}\text{Ne}/{}^{21}\text{Ne}$ (here measured = cosmogenic), with the data tables given by Leya and Masarik (2009). We used the more precise $({}^{22}\text{Ne}/{}^{21}\text{Ne})_{\text{cos}} = 1.0826 \pm 0.0026$ from Stubenberg I. The found mass of 1470 g corresponds to a radius of only 4.7 cm, with a density for LL chondrites of 3.29 g cm^{-3} (Wilkison and Robinson 2000). However, the preatmospheric mass has been determined to be 600 kg (Spurný et al. 2016). This limits the maximum radius conservatively to 45 cm (corresponding to 1200 kg mass). Based on $({}^{22}\text{Ne}/{}^{21}\text{Ne})_{\text{cos}}$ and the Leya and Masarik (2009) model, the minimum radius is 35 cm. The production rates and the uncertainties given in the table cover all values allowed in this range.

Table 8. “Shielding indicator” cosmogenic ${}^{22}\text{Ne}/{}^{21}\text{Ne}$, CRE, and nominal gas-retention ages.

	$({}^{22}\text{Ne}/{}^{21}\text{Ne})_{\text{cos}}$	T_3	T_{21}	T_{38}	T_{average}	U/Th- ${}^4\text{He}$	K- ${}^{40}\text{Ar}$
I	1.0826 ± 0.0026	37 ± 1	37 ± 1	39 ± 1	36 ± 3	2.99 ± 0.10	4.09 ± 0.08
II	1.05 ± 0.05	37 ± 1	37 ± 1	31 ± 1		3.06 ± 0.10	4.05 ± 0.09

CRE ages are in Ma, retention ages in Ga. T_{average} is the average of all six values including standard deviation. The larger scatter in the ${}^{38}\text{Ar}$ ages might be due to variations in Ca. Uncertainties do not include systematic uncertainties of the production rate determinations assumed to be typically 15–20% and uncertainties in the absolute gas calibrations (2% for He, Ne, Ar, and 5% for Kr, Xe; Heber et al. 2009).

-0.05 ± 0.11 , $\varepsilon^{50}\text{Ti} -0.67 \pm 0.09$; all uncertainties are 95% c.i.) and Zurich ($n = 7$; $\varepsilon^{46}\text{Ti} = -0.10 \pm 0.10$, $\varepsilon^{48}\text{Ti} = 0.00 \pm 0.03$, $\varepsilon^{50}\text{Ti} -0.81 \pm 0.09$) are within uncertainty identical to each other, and agree within error with literature values for ordinary chondrites (Trinquier et al. 2009; Zhang et al. 2012; Williams 2015) (Fig. S4 in supporting information).

Chromium Isotopes

The Cr isotope composition of Stubenberg is $\varepsilon^{53}\text{Cr} = 0.428 \pm 0.027$ and $\varepsilon^{54}\text{Cr} = -0.167 \pm 0.063$. The composition of $\varepsilon^{53}\text{Cr}$ is ~ 8 ppm higher than the previously highest value for ordinary chondrite (OC), while the $\varepsilon^{54}\text{Cr}$ value is within the range of previously reported OC compositions (e.g., Jenniskens et al. 2014; see Fig. 8). Although the Cr isotope composition of Stubenberg is on the extreme of the OC data array, its composition falls within the OC region when compared with other meteorite groups.

Solvent-Soluble Organic Matter

The analysis of the methanol-soluble organic fraction of Stubenberg by ultrahigh resolution mass spectrometry was undertaken in less than 24 h after the fragment was found on the field and in less than one week after its fall. For details on the significance of the analysis see Ruf et al. (2017). Care was taken with respect to differentiate indigenous organic matter and possible terrestrial contamination by analyzing corresponding solvent methanolic blanks (Schmitt-Kopplin et al. 2010). The main characteristics of the

compositional space was a high density of m/z signals (higher than 60 at each nominal mass) over a mass range from 150 to 650 amu (Fig. 9). These enormous number of m/z signals were annotated to molecular formulas with respect to C-, H-, N-, O-, S- and Mg-bearing compositions. The CHO, CHOMg, and CHNO compositions rule the detected soluble organic space of the Stubenberg meteorite.

Physical Characteristics

FTIR Spectroscopy

The analyzed polished thin sections and rough, unprepared surfaces of the Stubenberg samples show similar spectra compared with those obtained from other metamorphosed LL-group chondrites. The FTIR spectra in the mid-infrared of polished thin sections and rough surfaces show very similar features (Figs. 10 and S5 in supporting information). The characteristic Christiansen feature (CF), a reflectance minimum used to estimate bulk compositions in remote sensing (Salisbury 1993) is at $7.9\text{--}8.1 \mu\text{m}$. The strongest Reststrahlen b and (RB) is a “twin-peak” feature at $10.8 \mu\text{m}$ and $11.3 \mu\text{m}$ of two bands with comparable intensity. Further strong RB are overlapping olivine, pyroxene, and plagioclase features found at 9.1 , 9.6 , 10.3 , and $12.0 \mu\text{m}$, and at 13.8 , 14.6 , 15.6 , and $16.7 \mu\text{m}$ at longer wavelengths (Hamilton 2000, 2010; Baldrige et al. 2009).

At shorter wavelengths, bands at $2.9 \mu\text{m}$ indicate probably adsorbed terrestrial water. Weak features at

Table 9. Massic activities (corrected to the fall of the meteorite March 6, 2016) of cosmogenic radionuclides (in dpm kg⁻¹) in the specimens M1b and M5 of the Stubenberg stone measured by nondestructive gamma-ray spectroscopy. Errors include a 1 σ uncertainty of 10% in the detector efficiency calibration (n.d. = not determined).

Nuclide	Half-life	Stubenberg	
		M1b (23.58 g)	M5 (1320 g)
⁴⁸ V	15.9735 d	18 ± 2	n.d.
⁵¹ Cr	27.704 d	32 ± 9	n.d.
⁷ Be	53.22 d	74 ± 10	85.4 ± 8.8
⁵⁸ Co	70.83 d	4.1 ± 0.7	4.7 ± 0.6
⁵⁶ Co	77.236 d	4.0 ± 0.7	4.5 ± 0.6
⁴⁶ Sc	83.787 d	7.6 ± 0.8	6.8 ± 0.7
⁵⁷ Co	271.8 d	4.9 ± 0.9	6.0 ± 1.0
⁵⁴ Mn	312.3 d	55.1 ± 5.7	60.9 ± 4.7
²² Na	2.60 y	86.6 ± 9.0	87.0 ± 6.7
⁶⁰ Co	5.27 y	0.9 ± 0.3	<0.5
⁴⁴ Ti	60 y	<4.8	n.d.
²⁶ Al	7.17 × 10 ⁵ y	60.7 ± 4.8	57.4 ± 4.4

3.4 and 3.5 μm could be aliphatic C-H stretching of CH₂ and CH₃. Bands at 5.7–6 μm could be also due to water, but overlap with C=O stretching modes (Kebukawa et al. 2011).

Magnetic Susceptibility

The average values for the magnetic susceptibility (MS) of the samples, corrected for mass and dimensions, are given in Table 10. The correction procedure produces consistent values over three orders of magnitude of the sample mass as shown in Fig. S6 in supporting information. For the conversion of volumetric MS instrument readings into MS the bulk density of 3.29 g cm⁻³ was used.

The overall average of MS is about 4.800*10⁻⁹m³ kg⁻¹ corresponding to log(MS) = 3.68 which places Stubenberg at the low end of the range for LL chondrites (Table 10). The 95% confidence interval of ± 0.03 for log(MS) containing both the experimental scattering and the material inhomogeneity is remarkably narrow. The variability of five measurements at different portions of the main mass (M5) is approximately the same as that of those across all samples indicating a quite homogeneous distribution of metal in the breccia.

DISCUSSION

Mineralogical Properties and Classification of Stubenberg

Stubenberg is a breccia based on presented results. The textures of individual fragments are highly recrystallized (Fig. 3) and only a few relic chondrules are

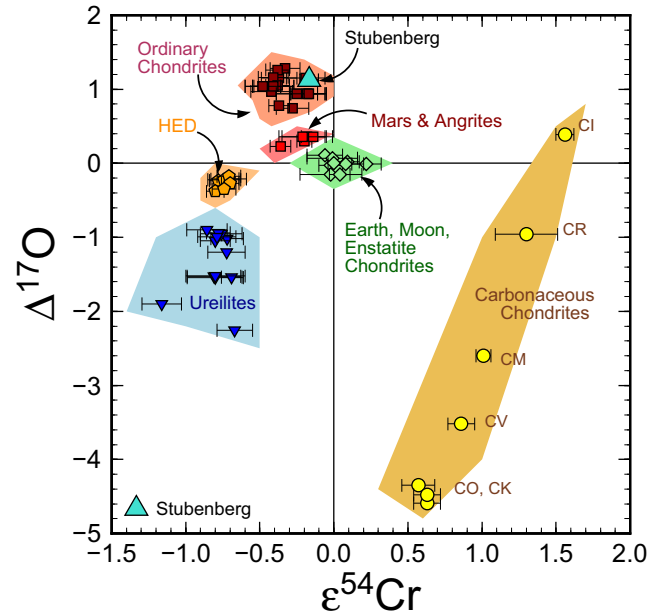


Fig. 8. Chromium and oxygen isotopes of Stubenberg in the $\epsilon^{54}\text{Cr}$ - $\Delta^{17}\text{O}$ isotope diagram compared with other meteorites groups. Different meteorite groups define tight clusters, which imply that they either originate from the same parent bodies or they formed from similar materials. Stubenberg falls within the ordinary chondrite field. Data are from: Clayton and Mayeda (1984, 1996, 1999); Clayton et al. (1991); Wiechert et al. (2004); Shukolyukov and Lugmair (2006); Ueda et al. (2006); Trinquier et al. (2008); Qin et al. (2010); Yamakawa et al. (2010); Popova et al. (2013); Rumble et al. (2010); Jenniskens et al. (2014).

visible in thin section (Fig. 3). These observations already point to a high metamorphic grade of the fragments within the rock. The large grain size of plagioclase and the homogeneous compositions of olivines and pyroxenes also support this. These facts clearly indicate that the fragments within Stubenberg are of type 6. Based on the mean olivine and low-Ca pyroxene compositions of Fa_{31.4} and Fs_{25.4}, respectively, the rock has to be classified as an LL-group ordinary chondrite breccia. Since no fragments of other petrologic type have been observed so far a classification as a LL6 breccia is appropriate. However, Stubenberg does not belong to the complicated breccias like Almahata Sitta (e.g., Bischoff et al. 2010; Horstmann et al. 2010; Goodrich et al. 2014; Horstmann and Bischoff 2014) or to the complex regolith breccias among the L- and LL-group ordinary chondrites (Bischoff et al. 1993, 2006, 2013a; Metzler et al. 2010, 2011) and is also different to the LL5-6 breccia Chelyabinsk (Bischoff et al. 2013b; Righter et al. 2015; Morlok et al. 2017). This is consistent with the lack of solar wind implanted noble gases (Fig. 7); thus, the breccia does not contain fragmental debris that was exposed at the surface and hence has to be characterized

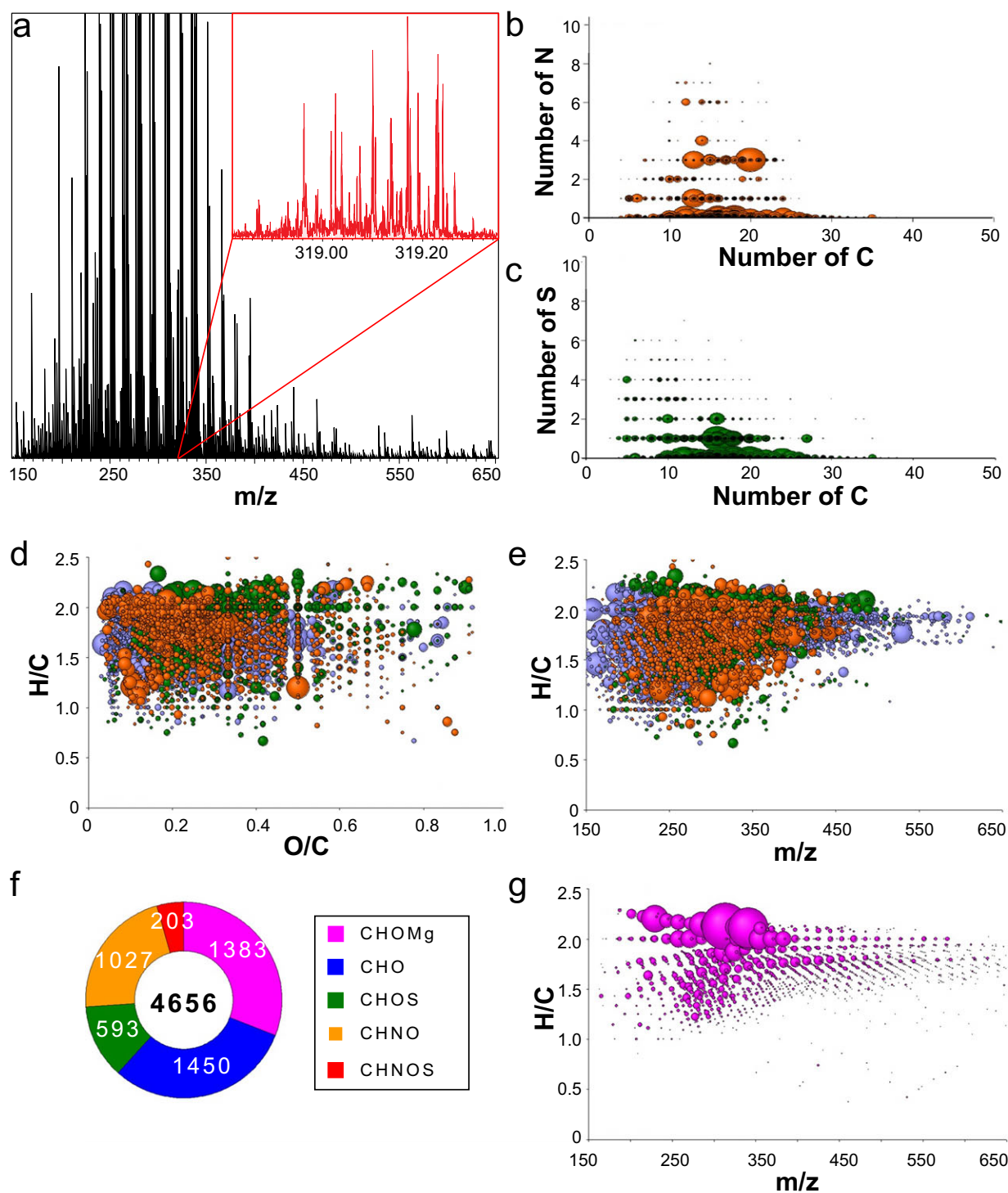


Fig. 9. Negative electrospray ionization mode (ESI) Fourier transform ion cyclotron resonance mass spectrometry ((-) ESI-FT-ICR-MS) FT-ICR-MS analysis of methanolic extracts revealed ~4600 elementary compositions in the CHNMgOS space. Part (a) illustrates the mass profile in the range 150–650 amu with a zoomed-in detail on the high chemodiversity, as shown exemplarily for the nominal mass 319. This enlarged mass range shows more than 70 m/z signals. Panel (b), (c): The number of nitrogen and sulfur atoms in the molecular compositions is shown as a function of the number of carbon atoms. Additionally, the soluble organic compositions are depicted in van Krevelen diagram-type representations of the data with additional extension of the CHNOS space (d and e) and the CHOMg space (g). The bubble size represents the relative intensity of the mass peaks and each data point is related to one molecular formula. Panel (f) depicts the distribution of the chemical subspaces CHOMg, CHO, CHOS, CHNO, and CHNOS.

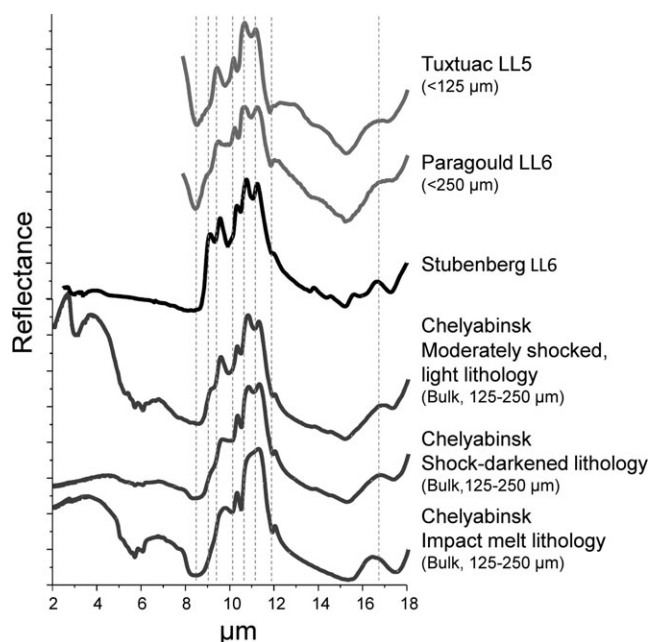


Fig. 10. Midinfrared spectrum of Stubenberg (in black) compared to other LL chondrites Tuxtuac and Paragould (on top) and various Chelyabinsk lithologies (bottom; Morlok et al. 2017). Vertical lines mark characteristic features. Stubenberg does not show the loss of feature strengths exhibited by the Chelyabinsk lithologies resulting from shock metamorphism, thus indicating a generally low degree of impact shock.

as a fragmental breccia. This result is also consistent with the observation that no other lithologies beside type 6 fragments were encountered. Considering the onion-shell model for the setting of the parent body no clasts of lower petrologic type (3–5) originated from the upper areas of the parent body were mixed into the breccia during impact-induced lithification (Kieffer 1975; Bischoff et al. 1983).

Based on the undulatory extinction in olivine and plagioclase and the presence of planar fractures in olivine, the chondrite is weakly shocked (S3). Thus, Stubenberg is an LL6, S3 ordinary chondrite breccia.

Applying the two-pyroxene thermometer implemented in the QUILF 95 program (Andersen et al. 1993) using the compositions listed in Table 2 yields an equilibration temperature of $914 \pm 44^\circ\text{C}$. This is consistent with typical values obtained from LL6 chondrites and interpreted as peak metamorphic temperatures (Slater-Reynolds and McSween 2005). Ni-poor pentlandite has been described from several equilibrated LL chondrites and the coexistence of pentlandite with troilite, kamacite, taenite, and potentially tetrataenite indicates disequilibrium among these opaque phases (Michel-Lévy and Bourot Denise 1992; Jamsja and Ruzicka 2010). The low Ni content places the pentlandite outside of the typical compositional range observed in

exsolved pentlandite-pyrrhotite assemblages (e.g., Jamsja and Ruzicka 2010), but thermodynamic modeling suggests that (partial) equilibration at temperatures below 360°C will produce Fe-rich pentlandite (Waldner and Pelton 2004). Disregarding the Co content, the pentlandite may have last equilibrated with the troilite at a temperature of about 250°C or below. Possibly, the sulfide assemblage was produced and incorporated during the brecciation event and internally equilibrated during cooling without significant chemical exchange with the other opaque phases of the rock.

Two different TiO_2 phases (anatase and rutile) could be identified as single grains by their different Raman spectra (Fig. S2). Ramdohr (1973) proposed the following reaction concerning a likely Ti-oxide formation process in ordinary chondrites: Reduction of ilmenite in the presence of carbon phases (carbon, graphite, or hydrocarbons), which have been also detected in Stubenberg (see above) to native iron and Ti-oxide according to the reaction: $2\text{FeTiO}_3 + \text{C} = 2\text{Fe} + 2\text{TiO}_2 + \text{CO}_2$.

Chemical Properties of Stubenberg

The bulk composition of the Stubenberg meteorite determined so far is very close to the published concentrations of other metamorphosed LL-group ordinary chondrites like Chelyabinsk (Table 3; Fig. 6; Righter et al. 2015). It can be concluded that no anomalies in elemental composition of the Stubenberg meteorite were detected compared with other LL chondrites. The O, Ti, and Cr isotope compositions of Stubenberg are also typical of LL ordinary chondrites (Figs. 8, S3, and S4).

Exact molecular formula assignments and resulting compositional space of organic constituents show a consistent coverage of ~ 4600 elementary compositions. In van Krevelen-type representations, the chemical space is plotted as H/C versus O/C ratio or m/z ratio (Fig. 9) keeping abundances of the signals in bubble sizes. This allows insights on the chemical properties on the plotted chemical compositions. Information regarding the degree of unsaturation and oxygenation about the respective chemical compositions are observed, detecting a broad range of oxygenation of mainly aliphatic compounds for the Stubenberg soluble organic matter. Compositions with higher degree of oxidation and higher number of nitrogen and sulfur could be observed, as compared to lower shock-metamorphosed ordinary chondrites (Fig. 9; Schmitt-Kopplin et al. 2012; Popova et al. 2013; Jenniskens et al. 2014). High shock-metamorphosed ordinary chondrites show higher nitrogenated chemical compounds (Popova et al. 2013; Jenniskens et al. 2014). In addition, Stubenberg showed an unusual organomagnesium space (CHOMg) with an extremely dense and complete signature with more than 1000

Table 10. Magnetic susceptibility (MS) of representative individuals and fragments of the Stubenberg fall (compare Table 1) and of LL meteorites (falls only) from the literature for comparison: (1) Rochette et al. (2003); (2) Macke (2010). N = number of analyzed LL chondrites.

Sample	Mass [g] or N	MS [$10^{-9} \text{ m}^3 \text{ kg}^{-1}$]	log MS [$10^{-9} \text{ m}^3 \text{ kg}^{-1}$]	Ref.
M1c	1.834	4668	3.669	This study
M1n	2.289	4764	3.678	This study
M2a	7.212	4889	3.689	This study
M3	19.236	5076	3.705	This study
M5	1320	4723	3.674	This study
M6	35.887	4728	3.675	This study
Average		4817 ± 172	3.683 ± 0.015	This study
LL 3	8		4.37 (4.03–4.67)	(1)
	5		4.38 (4.19–4.57)	(2)
LL 4	5		4.18 (3.58–4.43)	(1)
	5		4.27 (3.61–4.66)	(2)
LL 5	12		4.13 (3.70–4.54)	(1)
	6		4.21 (3.83–4.65)	(2)
LL 6	19		3.95 (3.56–4.27)	(1)
	16		3.93 (3.46–4.71)	(2)
LL 7	1 (Uden)		3.33	(1)

CHOMg compositions, as many as CHO compositions. This reflects a high metamorphic temperature and a complex shock history of the parent body as explained in detail elsewhere (Ruf et al. 2017) as these thermostable metalorganic compounds could be related to the degree of thermal process of a meteorite. From the rapid results obtained on the soluble organic compositions, we conclude that Stubenberg shows characteristics consistent with the complex shock, brecciation, and lithification history of the breccia.

As expected for a freshly fallen LL6 chondrite, the noble gases do not carry significant terrestrial contamination. All precisely measurable heavier noble gas element and isotopic ratios indicate pure meteoritic rather than terrestrial noble gases. The trapped ^{36}Ar , ^{84}Kr , and ^{132}Xe concentrations are extremely low, consistent with Stubenberg being classified in this work as LL6. For example, element ratios and isotopic compositions (particularly $^{40}\text{Ar}/^{36}\text{Ar}$ and $^{129}\text{Xe}/^{132}\text{Xe}$) are similar to those found in LL5 Olivenza and LL6 Saint Séverin (Alaerts et al. 1979). The trapped gases that remained after thermal metamorphism are similar to phase Q gases (Busemann et al. 2000). The presence of ^{129}Xe derived from short-lived ^{129}I with a half-life of ~ 16 Ma ($^{129}\text{Xe}/^{132}\text{Xe} = 1.90$ and 1.95) indicates closure for Xe loss within the first ~ 100 Ma.

We obtain a most likely 4π CRE age for Stubenberg of 36 ± 3 Ma assuming a radius of 35–50 cm (covering all shielding conditions “allowed” by the cosmogenic $^{22}\text{Ne}/^{21}\text{Ne}$ of 1.0826 determined for Stubenberg; Leya and Masarik 2009). This age is an average of all six CRE ages obtained for both samples and the three light cosmogenic isotopes ^3He , ^{21}Ne , and

^{38}Ar (Table 4). This age is typical for a large fraction of LL chondrites with CRE ages around 30 Ma (e.g., Scherer et al. 1998; fig. 4 in Herzog and Caffee 2014). Much larger preatmospheric radii, while still possible using noble gas systematics alone, might not be likely, based on the preatmospheric mass of 600 kg as estimated with fireball observations (Spurný et al. 2016).

The remarkable agreement between all CRE ages (Table 4) suggests no preferred He loss due to heating in space (as a possible result of the meteoroid’s passage close to the Sun), or during atmospheric entry, which could cause preferential He loss. This observation allows us to also determine gas-retention ages for Stubenberg, unaffected by late reset, after ejection from the LL parent body. Using the K, U, and Th concentrations determined in this work (Table 3), we obtain nominal (maximum) U/Th- ^4He ages of ~ 3.0 Ga and K- ^{40}Ar ages of ~ 4.1 Ga (Table 4). The measured U concentration of 6.3 ppm appears somewhat low (Table 3). If we use a more typical U concentration of 13 ppm (e.g., Wasson and Kallemeyn 1988), the U/Th- ^4He ages would be around 2.2 Ga.

Such gas-retention ages can be determined under the assumption that significant partial loss after the calculated closure to gas loss did not occur. Such nominal ages have been observed for LL chondrites before, and show generally that the material of Stubenberg has not been shocked severely late in the LL chondrite parent body’s history.

^{26}Al (Leya and Masarik 2009), ^{60}Co (Eberhardt et al. 1963; Spergel et al. 1986), ^{54}Mn (Kohman and Bender 1967), and ^{22}Na (Bhandari et al. 1993) give as possible size range of the parent body (in the sequence

of the given isotopes) radii of 20–120 cm, <20 cm, 10–126 cm, and 15–100 cm. Combining all results of these radionuclides we infer a roughly spherical meteoroid with <20 cm radius, mainly due to the very small value of ^{60}Co . This estimate is further confirmed by the fact that the values for both specimens, so different in size, are similar (see Bhandari et al. 1993). The $^{22}\text{Na}/^{26}\text{Al}$ of (1.5 ± 0.2) is close to the average value for LL chondrites (Bhandari et al. 2002).

The fall of the Stubenberg LL6 chondrite occurred during the current solar cycle 24 maximum, as indicated by the neutron monitor data (Bartol Neutron Monitors 2016). The cosmic ray flux was low in the 6 months before the fall. As a result, the activities for the very short-lived radionuclides are expected to be low (see Table 5), similar to the earlier reported data for Jesenice (Bischoff et al. [2011] and references cited therein). The naturally occurring radionuclides (Table S3) are in agreement with the average concentrations in ordinary LL chondrites (Wasson and Kallemeyn 1988).

The calculated difference in radius resulting from short-lived radionuclides (<20 cm) and noble gases (>35 cm) could be explained if Stubenberg experienced a complex exposure history, in which most of the cosmogenic noble gases were produced in a >35 cm object in space, before a collision reduced the meteoroid size to <20 cm. Since the ^{26}Al data are consistent with a larger (20–120 cm radius; Leya and Masarik 2009) object, the change in radius would have to have happened within no more than a few half-lives of ^{26}Al ($t_{1/2} = 717$ ka). A complex exposure history for Stubenberg would also seem likely because its CRE age is a factor three to four times longer than the typical time such a small meteoroid is likely to escape collisional disruption in the asteroid belt, of 9 and 12 Ma for an $R = 20$ cm and $R = 35$ cm stony meteoroid, respectively (Farinella et al. 1998). However, there is an additional discrepancy between the size of Stubenberg as implied by short-lived radionuclides (<20 cm) and the estimated mass of the meteoroid implied from fireball observations (approximately 600 kg, $R \sim 35$ cm; Spurný et al. 2016). This could potentially be resolved if the Stubenberg meteoroid had a significant macroporosity: as the cosmic ray-induced production of cosmogenic noble gases and radionuclides depends on the product of radius and density, a lower bulk density would result in a larger physical radius and thus a much larger mass (since $M \sim R^3$; see Welten et al. 2010). At a fragment density of 3.29 g cm^{-3} and a macroporosity of 50%, a meteoroid with a size consistent with the measured ^{60}Co activity would have a mass of ~ 530 kg, consistent with the mass from the fireball estimate. More detailed modeling of the entry fireball, which is beyond the scope of this paper, will be required to resolve this discussion.

Physical Properties of Stubenberg

The analyzed polished thin sections and rough, unprepared surfaces of the Stubenberg samples show similar spectra compared with those obtained from other metamorphosed LL-group chondrites (Figs. 10 and S5), Tuxtuac (LL5) and Paragould (LL6). These spectra were acquired by investigators Carle Pieters and Jitendra N. Goswami with the NASA RELAB facility at Brown University. They show essentially similar RB features at 9.5–9.6, 10.3, 10.8, and 11.2–11.3 μm as Stubenberg, while the CF is clearly shifted with 8.6 μm compared to 8.0–8.1 μm for Stubenberg, indicating a lower content in crystallized mesostasis feldspar (Fig. 10) (Salisbury 1993).

The comparison of the FTIR data with that of heavily shocked LL6 chondrite Chelyabinsk (Morlok et al. 2017) shows a high similarity in band positions and band shapes with the moderately shocked lithology (Fig. 10). In addition to the four strong bands between 9.6 and 11.3 μm , which are also visible in the moderately shocked lithology of Chelyabinsk, Stubenberg also has a clear feature at 9.1 μm , which is only visible as a shoulder in the Chelyabinsk samples. Shock-darkened and impact melt lithologies show a decrease in feature intensities and loss of bands. This implies a low degree of impact shock of the bulk Stubenberg material. Features visible in the 5.7–6.0 μm range occurring in the Chelyabinsk sample are only very weak in Stubenberg. This is most probably due to the differences in sample preparation, where the powdered Chelyabinsk material provided higher surface area resulting in stronger minor features compared to the surfaces analyzed of Stubenberg in this work.

The measured magnetic susceptibility data support the classification of Stubenberg as an LL chondrite. Comparing the average values of LL-group members given in Rochette et al. (2003) and Macke (2010) the Stubenberg value is significantly lower than the data of LL3 to LL6 meteorites. On the other hand, regarding the limits of variation in the different groups, Stubenberg might fit into LL4 to LL6, with a tendency toward the very special LL7 group (however, represented only by one measured fall, Uden) with a still lower susceptibility value (3.33).

CONCLUSION

Stubenberg fell on March 6, 2016 and the first pieces were recovered 6 days later after an exact calculation of the impact area based on instrumental observations taken by the six cameras of the Czech part of the European Fireball Network. Altogether six individuals weighing in total 1473 g were recovered. It

is classified as an LL6, S3 ordinary chondrite fragmental breccia. The bulk composition of the Stubenberg meteorite is very close to element concentrations of other metamorphosed LL-group ordinary chondrites. This is also consistent with O, Ti, and Cr isotope data and IR spectroscopy.

The measured activities of short-lived cosmogenic radionuclides clearly indicate that the analyzed pieces result from a very recent meteorite fall consistent with the Stubenberg fall. A cosmic ray exposure (CRE) age of 36 ± 3 Ma has been obtained for the meteoroid. Using the K, U, and Th concentrations determined in this work nominal (maximum) U/Th- ^4He ages of ~ 3.0 Ga and K- ^{40}Ar ages of ~ 4.1 Ga are determined.

Acknowledgments—We thank U. Heitmann (Münster) and M. Lippold (Jena) for sample preparation. Christian Rewitzer (München) is thanked by one of the authors (RH) for making his scanning electron microscope available for investigations of the Stubenberg meteorite. We thank C. Corrigan, an anonymous reviewer, and the Associate Editor Ed Scott for their fruitful comments and suggestions. The SEM-FIB-TEM facility at the Universität Jena is funded by the DFG (grant LA 830/14-1); F. Langenhorst is thanked for support of the work conducted at the facility. The work of P. Spurný was supported by Praemium Academiae from the Czech Academy of Sciences. M. M., K. B., and M. S. thank the Swiss National Science Foundation (SNF) for support. A. B. and S. E. thank the DFG for support within the SFB-TRR 170 “Late Accretion onto Terrestrial Planets” (subproject B5; AB). This is TRR 170 publication No. 23. This work was partly supported (AM, HH) by DLR grant 50 QW 1302 in the framework of the BepiColombo mission. This research utilizes spectra acquired by C.M. Pieters and J.M. Sunshine with the NASA RELAB facility at Brown University. This publication is contribution (5322) of the University of Maryland Center for Environmental Science. The samples were donated by Michael Krippner, Michael Gonsior, Dennis Harries, Ralph Sporn, and Martin Neuhofer. This is greatly acknowledged.

Editorial Handling—Dr. Edward Scott

REFERENCES

- Alaerts L., Lewis R. S., and Anders E. 1979. Isotopic anomalies of noble gases in meteorites and their origins—III. LL-chondrites. *Geochimica et Cosmochimica Acta* 43:1399–1415.
- Andersen D. J., Lindsley D. H., and Davidson P. M. 1993. QUILF: A Pascal program to assess equilibria among Fe-Mg-Mn-Ti oxides, pyroxenes, olivine, and quartz. *Computers & Geosciences* 19:1333–1350.
- Arpesella C. 1996. A low background counting facility at Laboratori Nazionali del Gran Sasso. *Applied Radiation and Isotopes* 47:991–996.
- Baldrige A. M., Hook S. J., Grove C. I., and Rivera G. 2009. The ASTER spectral library version 2.0. *Remote Sensing of Environment* 113:711–715.
- Barrat J.-A., Zanda B., Moynier F., Bollinger C., Liorzou C., and Bayron G. 2012. Geochemistry of CI chondrites: Major and trace elements, and Cu and Zn isotopes. *Geochimica et Cosmochimica Acta* 83:79–92.
- Barrat J.-A., Rouxel O., Wang K., Moynier F., Yamaguchi A., Bischoff A., and Langlade J. 2015. Early stages of core segregation recorded by Fe isotopes in an asteroidal mantle. *Earth and Planetary Science Letters* 419:93–100.
- Barrat J.-A., Gillet P., Dauphas N., Bollinger C., Etoubleau J., Bischoff A., and Yamaguchi A. 2016. Evidence from Tm anomalies for non-CI refractory lithophile element proportions in terrestrial planets and achondrites. *Geochimica et Cosmochimica Acta* 176:1–17.
- Bartol Neutron Monitors. 2016. <http://neutronm.bartol.udel.edu/>
- Bartoschewitz R., Appel P., Barrat J.-A., Bischoff A., Caffee M. W., Franchi I. A., Gabelica Z., Greenwood R. C., Harir M., Harries D., Hochleitner R., Hopp J., Laubenstein M., Mader B., Marques R., Morlok A., Nolze G., Prudêncio M. I., Rochette P., Ruf A., Schmitt-Kopplin P., Seemann E., Szurgot M., Tagle R., Wach R. A., Welten K. C., Weyrauch M., and Wimmer K. 2017. The Braunschweig meteorite—A recent L6 chondrite fall in Germany. *Chemie der Erde—Geochemistry*. doi:10.1016/j.chemer.2016.10.004.
- Bhandari N., Mathew K. J., Rao M. N., Herpers U., Bremer K., Vogt S., Wölfl W., Hofmann H. J., Michel R., Bodemann R., and Lange H.-J. 1993. Depth and size dependence of cosmogenic nuclide production rates in stony meteoroids. *Geochimica Cosmochimica Acta* 57:2361–2375.
- Bhandari N., Murty S. V. S., Shukla P. N., Shukla A. D., Mahajan R. R., Sarin M. M., Srinivasan G., Suthar K. M., Sisodia M. S., Jha S., and Bischoff A. 2002. Itawa Bhopji (L3-5) chondrite regolith breccia: Fall, classification and cosmogenic records. *Meteoritics & Planetary Science* 37:549–563.
- Bischoff A., and Stöffler D. 1992. Shock metamorphism as a fundamental process in the evolution of planetary bodies: Information from meteorites. *European Journal of Mineralogy* 4:707–755.
- Bischoff A., Rubin A. E., Keil K., and Stöffler D. 1983. Lithification of gas-rich chondrite regolith breccias by grain boundary and localized shock melting. *Earth and Planetary Science Letters* 66:1–10.
- Bischoff A., Geiger T., Palme H., Spettel B., Schultz L., Scherer P., Schlüter J., and Lkhamsuren J. 1993. Mineralogy, chemistry, and noble gas contents of Adzhi-Bogdo—An LL3-6 chondritic breccia with foreign clasts. *Meteoritics* 28:570–578.
- Bischoff A., Scott E. R. D., Metzler K., and Goodrich C. A. 2006. Nature and origins of meteoritic breccias. In *Meteorites and the early solar system II*, edited by Lauretta D. S. and McSween H. Y. Jr. Tucson, Arizona: University of Arizona. pp. 679–712.
- Bischoff A., Horstmann M., Pack A., Laubenstein M., and Haberer S. 2010. Asteroid 2008 TC₃—Almahata Sitta: A spectacular breccia containing many different ureilitic and chondritic lithologies. *Meteoritics & Planetary Science* 45:1638–1656.

- Bischoff A., Jersek M., Grau T., Mirtic B., Ott U., Kučera J., Horstmann M., Laubenstein M., Herrmann S., Randa Z., Weber M., and Heusser G. 2011. Jesenice—A new meteorite fall from Slovenia. *Meteoritics & Planetary Science* 46:793–804.
- Bischoff A., Dyl K. A., Horstmann M., Ziegler K., Wimmer K., and Young E. D. 2013a. Reclassification of Villalbeto de la Peña—Occurrence of a winonaite-related fragment in a hydrothermally metamorphosed polymict L-chondritic breccias. *Meteoritics & Planetary Science* 48:628–640.
- Bischoff A., Horstmann M., Vollmer C., Heitmann U., and Decker S. 2013b. Chelyabinsk—Not only another ordinary LL5 chondrite, but a spectacular chondrite breccia (abstract #5171). *Meteoritics & Planetary Science* 48:A61.
- Busemann H., Baur H., and Wieler R. 2000. Primordial noble gases in “phase Q” in carbonaceous and ordinary chondrites studied by closed-system stepped etching. *Meteoritics & Planetary Science* 35:949–973.
- Busemann H., Toth E. R., Clay P. L., Gilmour J. D., Nottingham M., Strashnov I., Wieler R., Nishiizumi K., and Jones R. H. 2014. Noble gases in the LL5 chondrite Chelyabinsk (abstract #2805). 45th Lunar Planetary Science Conference. CD-ROM.
- Clayton R. N. and Mayeda T. K. 1984. Oxygen isotopic compositions of enstatite chondrites and aubrites. *Journal of Geophysical Research* 89:C245–C249.
- Clayton R. N. and Mayeda T. K. 1996. Oxygen isotope studies of achondrites. *Geochimica et Cosmochimica Acta* 60:1999–2017.
- Clayton R. N. and Mayeda T. K. 1999. Oxygen isotope studies of carbonaceous chondrites. *Geochimica et Cosmochimica Acta* 63:2089–2104.
- Clayton R., Mayeda T., Olsen E., and Goswami J. 1991. Oxygen isotope studies of ordinary chondrites. *Geochimica et Cosmochimica Acta* 55:2317–2337.
- Eberhardt P., Geiss J., and Lutz H. 1963. Neutrons in meteorites. In *Earth science and meteoritics*, edited by Geiss J. and Goldberg E. D. Amsterdam: North Holland Publ. Co. pp. 143–168.
- Ebert S. and Bischoff A. 2016. The Stubenberg (Bavaria) ordinary chondrite breccia: The latest German meteorite fall (abstract #6137). *Meteoritics & Planetary Science* 51.
- Eugster O., Michel T., Niedermann S., Wang D., and Yi W. 1993. The record of cosmogenic, radiogenic, fissionogenic, and trapped noble gases in recently recovered Chinese and other chondrites. *Geochimica et Cosmochimica Acta* 57:1115–1142.
- Farinella P., Vokrouhlický D., and Hartmann W. K. 1998. Meteorite delivery via Yarkovsky orbital drift. *Icarus* 132:378–387.
- Goodrich C. A., Bischoff A. and O’Brien D. P. 2014. Asteroid 2008 TC₃ and the fall of Almahata Sitta, a unique meteorite breccia. *Elements* 10:31–37.
- Hamilton V. E. 2000. Thermal infrared emission spectroscopy of the pyroxene mineral series. *Journal of Geophysical Research* 105:9701–9716.
- Hamilton V. E. 2010. Thermal infrared (vibrational) spectroscopy of Mg-Fe olivines: A review and applications to determining the composition of planetary surfaces. *Chemie der Erde—Geochemistry* 70:7–33.
- Harries D. and Langenhorst F. 2013. The nanoscale mineralogy of Fe, Ni sulfides in pristine and metamorphosed CM and CM/C1-like chondrites: Tapping a petrogenetic record. *Meteoritics & Planetary Science* 48:879–903.
- Heber V. S., Wieler R., Baur H., Olinger C., Friedmann T. A., and Burnett D. S. 2009. Noble gas composition of the solar wind as collected by the Genesis mission. *Geochimica et Cosmochimica Acta* 73:7414–7432.
- Hertkorn N., Harir M., and Schmitt-Kopplin P. 2015. Nontarget analysis of Murchison soluble organic matter by high-field NMR spectroscopy and FTICR mass spectrometry. *Magnetic Resonance Chemistry* 53:754–768.
- Herzog G. F. and Caffee M. 2014. Cosmic-ray exposure ages of meteorites. In *Planets, asteroids, comets and the solar system*, edited by Davies A. M. Treatise on Geochemistry, Vol. 2. Boston: Elsevier. pp. 419–453.
- Heusser G., Weber M., Hakenmüller J., Laubenstein M., Lindner M., Maneschg W., Simgen H., Stolzenburg D., and Strecker H. 2015. GIOVE: A new detector setup for high sensitivity germanium spectroscopy at shallow depth. *The European Physical Journal C* 75:531.
- Heymann D. and Mazor E. 1966. St. Mesmin, a gas-rich amphoteric chondrite. *Journal of Geophysical Research* 71:4695–4697.
- Horstmann M. and Bischoff A. 2014. The Almahata Sitta polymict breccia and the late accretion of Asteroid 2008 TC₃—Invited review. *Chemie der Erde—Geochemistry* 74:149–184.
- Horstmann M., Bischoff A., Pack A., and Laubenstein M. 2010. Almahata Sitta—Fragment MS-CH: Characterization of a new chondrite type. *Meteoritics & Planetary Science* 45:1657–1667.
- Jamsja N. and Ruzicka A. 2010. Shock and thermal history of Northwest Africa 4859, an annealed impact-melt breccia of LL chondrite parentage containing unusual igneous features and pentlandite. *Meteoritics & Planetary Science* 45:828–849.
- Jenniskens P., Rubin A. E., Yin Q.-Z., Sears D. W. G., Sandford S. A., Zolensky M. E., Krot A. N., Blair L., Kane D., Utas J., Verish R., Friedrich J. M., Wimpenny J., Eppich G. R., Ziegler K., Verosub K. L., Rowland D. J., Albers J., Gural P. S., Grigsby B., Fries M. D., Matson R., Johnston M., Silber E., Brown P., Yamakawa A., Sanborn M. E., Laubenstein M., Welten K. C., Nishiizumi K., Meier M. M. M., Busemann H., Clay P., Caffee M. W., Schmitt-Kopplin P., Hertkorn N., Glavin D. P., Callahan M. P., Dworkin J. P., Wu Q., Zare R. N., Grady M., Verchovsky S., Emel’yanenko V., Naroenkov S., Clark D. L., Girten B., Worden P. S., and Consortium T. N. M. 2014. Fall, recovery, and characterization of the Novato L6 chondrite breccia. *Meteoritics & Planetary Science* 49:1388–1425.
- Kebukawa Y., Alexander C. M. O’D., and Cody G. D. 2011. Compositional diversity in insoluble organic matter in type 1, 2 and 3 chondrites as detected by infrared spectroscopy. *Meteoritics & Planetary Science* 75:3530–3541.
- Kieffer S. W. 1975. From regolith to rock by shock. *The Moon* 13:301–320.
- Kohman T. P. and Bender M. L. 1967. Nuclide production by cosmic rays in meteorites and on the Moon. In *High-energy nuclear reactions in astrophysics—A collection of articles*, edited by Shen B. S. P., New York: Benjamin W. A. pp. 169–245.
- Leya I. and Masarik J. 2009. Cosmogenic nuclides in stony meteorites revisited. *Meteoritics & Planetary Sciences* 44:1061–1086.
- Macke R. J. 2010. Survey of meteorite physical properties: density, porosity and magnetic susceptibility. PhD Thesis, University of Central Florida, Orlando.
- Meteoritical Bulletin Database*. 2017. <https://www.lpi.usra.edu/meteor/>. Accessed May 18, 2017.

- Metzler K., Bischoff A., Palme H., and Gellissen M. 2010. Impact melt rocks from the L3-6 chondritic regolith breccia Northwest Africa (NWA) 869. *Meteoritics & Planetary Science* 45:A137.
- Metzler K., Bischoff A., Greenwood R. C., Palme H., Gellissen M., Hopp J., Franchi I. A., and Trierloff M. 2011. The L3-6 chondritic regolith breccia Northwest Africa (NWA) 869: (I) Petrology, chemistry, oxygen isotopes, and Ar-Ar age determinations. *Meteoritics & Planetary Science* 46:652–680.
- Michel-Lévy M. C. and Bourot Denise M. 1992. Dahmani, a highly oxidised LL6 chondrite bearing Ni-rich taenite. *Meteoritics* 27:184–185.
- Morlok A., Bischoff A., Patzek M., Sohn M., and Hiesinger H. 2017. Chelyabinsk—A rock with many different (stony) faces: An infrared study. *Icarus* 284: 431–442.
- Pack A., Tanaka R., Hering M., Sengupta S., Peters S., and Nakamura E. 2016. The oxygen isotope composition of San Carlos olivine on VSMOW2-SLAP2 scale. *Rapid Communications in Mass Spectrometry* 30:1495–1504.
- Popova O. P., Jenniskens P., Emelyanenko V., Kartashova A., Biryukov E., Khaibrakhmanov S., Shuvalov V., Rybnov Y., Dudorov A., Grokhovskiy V. I., Badyukov D. D., Yin Q.-Z., Gural P. S., Albers J., Granvik M., Evers L. G., Kuiper J., Kharlamov V., Solovyov A., Rusakov Y. S., Korotkiy S., Serdyuk I., Korochantsev A. V., Larionov M. Y., Glazachev D., Mayer A. E., Gisler G., Gladkovsky S. V., Wimpenny J., Sanborn M. E., Yamakawa A., Verosub K. L., Rowland D. J., Roeske S., Botto N. W., Friedrich J. M., Zolensky M. E., Le L., Ross D., Ziegler K., Nakamura T., Ahn I., Lee J. I., Zhou Q., Li X.-H., Li Q.-L., Liu Y., Tang G.-Q., Hiroi T., Sears D., Weinstein I. A., Vokhmintsev A. S., Ishchenko A. V., Schmitt-Kopplin P., Hertkorn N., Nagao K., Haba M. K., Komatsu M., and Mikouchi T. 2013. Chelyabinsk airburst, damage assessment, meteorite recovery, and characterization. *Science* 342:1069–1073.
- Qin L., Alexander C. M. O'D., Carlson R. W., Horan M. F., and Yokoyama T. 2010. Contributors to chromium isotope variation of meteorites. *Geochimica et Cosmochimica Acta* 74:1122–1145.
- Ramdohr P. 1973. *The opaque minerals in stony meteorites*. London: Elsevier Publishing Company. 245 pp.
- Riebe M. E. I., Welten K., Meier M. M. M., Wieler R., Bart M. I. F., Ward D., Laubenstein M., Bischoff A., Caffee M. W., Nishiizumi K., and Busemann H. Forthcoming. Cosmic-ray exposure ages of six chondritic Almahata Sitta fragments. *Meteoritics & Planetary Science*.
- Righter K., Abell P., Agresti D., Berger E. L., Burton A. S., Delaney J. S., Fries M. D., Gibson E. K., Haba M. K., Harrington R. F., Herzog G. F., Keller L. P., Locke D., Lindsay F. N., McCoy T. J., Morris R. V., Nagao K., Nakamura-Messenger K., Niles P. B., Nyquist L. E., Park J., Peng Z. X., Shih C.-Y., Simon J. I., Swisher III C. C., Tappa M. J., Turrin B. D., and Zeigler R. A. 2015. Mineralogy, petrology, chronology, and exposure history of the Chelyabinsk meteorite and parent body. *Meteoritics & Planetary Science* 50:1790–1819.
- Rochette P., Sagnotti L., Bourot-Denise M., Consolmagno G., Folco L., Gattacceca J., Osete M. L., and Pesonen L. 2003. Magnetic classification of stony meteorites: 1. Ordinary chondrites. *Meteoritics & Planetary Science* 38:251–268.
- Ruf A., Kanawati B., Hertkorn N., Yin Q. Z., Moritz F., Harir M., Lucio M., Michalke B., Wimpenny J., Shilobreeva S., Bronsky B., Saraykin V., Gabelica Z., Gougeon R., Quirico E., Ralew S., Jakubowski T., Haack H., Jenniskens P., Hinman N. W., and Schmitt-Kopplin P. 2017. Previously unknown class of metalorganic compounds revealed in meteorites. *Proceedings of the National Academy of Sciences* 114: 2819–2824. doi:10.1073/pnas.1616019114
- Rumble D., Zolensky M. E., Friedrich J. M., Jenniskens P., and Shaddad M. H. 2010. The oxygen isotope composition of Almahata Sitta. *Meteoritics & Planetary Science* 45:1765–1770.
- Salisbury J. W. 1993. Mid-infrared spectroscopy: Laboratory data. In: *Remote geochemical analysis: Elemental and mineralogical composition*, edited by Pieters C. M. and Englert P. A. J. Cambridge: Cambridge University Press. pp. 79–98.
- Scherer P., Herrmann S., and Schultz L. 1998. Noble gases in twenty-one Saharan LL-chondrites: Exposure ages and possible parings. *Meteoritics & Planetary Science* 33:259–265.
- Schmitt-Kopplin P., Gabelica Z., Gougeon R. D., Fekete A., Kanawati B., Harir M., Gebefuegi I., Eckel G., and Hertkorn N. 2010. High molecular diversity of extraterrestrial organic matter in Murchison meteorite revealed 40 yr after its fall. *Proceedings of the National Academy of Sciences* 107:2763–2768.
- Schmitt-Kopplin P., Harir M., Kanawati B., Tziotis D., Hertkorn N., and Gabelica Z. 2012. Chemical footprint of the solvent soluble extraterrestrial organic matter occluded in Soltmany ordinary chondrite. *Meteorite Journal, Special issue Soltmany* 1–2:79–92.
- Schönbächler M., Rehkämper M., Lee D.-C., and Halliday A. N. 2004. Ion exchange chromatography and high precision isotopic measurements of zirconium by MC-ICP-MS. *Analyst* 129:32–37.
- Schultz L. and Franke L. 2004. Helium, neon, and argon in meteorites: A data collection. *Meteoritics & Planetary Science* 39:1889–1890.
- Sharp Z. D. 1990. A laser-based microanalytical technique for in situ determination of oxygen isotope ratios of silicates and oxides. *Geochimica et Cosmochimica Acta* 54:1353–1357.
- Shukolyukov A. and Lugmair G. W. 2006. Manganese-chromium isotope systematics of carbonaceous chondrites. *Earth and Planetary Science Letters* 250:200–213.
- Slater-Reynolds V. and McSween H. Y. 2005. Peak metamorphic temperatures in type 6 ordinary chondrites: An evaluation of pyroxene and plagioclase geothermometry. *Meteoritics & Planetary Science* 40:745–754.
- Spergel M. S., Reedy R. C., Lazareth O. W., Levy P. W., and Slate L. A. 1986. Cosmogenic neutron-capture-produced nuclides in stony meteorites. 16th Proceedings of the Lunar & Planetary Science Conference. *Journal of Geophysical Research* 91:D483–D494.
- Spurný P. 2016. Instrumentally documented meteorite falls: two recent cases and statistics from all falls. In *Asteroids: New observations, new models*, edited by Chesley S. R., Morbidelli A., Jedicke R., and Farnocchia D. *IAU Symposium*. 318:69–79.
- Spurný P., Borovička J., and Shrubený L. 2007. Automation of the Czech part of the European fireball network: Equipment, methods and first results. In *Near Earth objects, our celestial neighbors: Opportunity and risk*, edited by Milani A., Valsecchi G. B., and Vokrouhlický D. IAU Symposium. Cambridge: Cambridge University Press. pp. 121–130.
- Spurný P., Borovička J., Haloda J., Shrubený L., and Heinlein D. 2016. Two very precisely instrumentally documented meteorite falls: Žďár nad Sázavou and Stubenberg – prediction and reality (abstract # 6221). *Meteoritics & Planetary Science* 51.

- Steele R. C. J. and Schönbächler M. 2016. High precision mass-independent Cr isotope compositions by MC-ICPMS and MC-TIMS: Application to terrestrial and meteorite samples. *Goldschmidt abstract*, #2947.
- Stöffler D., Keil D., and Scott E. R. D. 1991. Shock metamorphism of ordinary chondrites. *Geochimica et Cosmochimica Acta* 55:3845–3867.
- Trinquier A., Birk J. L., Allègre C. J., Göpel C., and Ulfbeck D. 2008. ^{53}Mn – ^{53}Cr systematics of the early solar system revisited. *Geochimica et Cosmochimica Acta* 72:5146–5163.
- Trinquier A., Elliott T., Ulfbeck D., Coath C., Krot A. N., and Bizzarro M. 2009. Origin of nucleosynthetic isotope heterogeneity in the solar protoplanetary disk. *Science* 324:374–376.
- Tziotis D., Hertkorn N., and Schmitt-Kopplin P. 2011. Kendrick-analogous network visualisation of ion cyclotron resonance Fourier transform (FTICR) mass spectra: Improved options to assign elemental compositions and to classify organic molecular complexity. *European Journal of Mass Spectrometry* 17:415–421.
- Ueda T., Yamashita K., and Kita N. 2006. Chromium isotopic study of ureilite. *Meteoritics and Planetary Science* 41:5178.
- Waldner P. and Pelton A. D. 2004. Thermodynamic modeling of the Ni-S system. *Zeitschrift für Metallkunde* 95:672–681.
- Wasson J. T. and Kallemeyn G. W. 1988. Compositions of chondrites. The solar system: Chemistry as a key to its origin. *Philosophical Transactions of the Royal Society of London. Series A, Mathematical and Physical Sciences* 325:535–544.
- Welten K. C., Meier M. M. M., Caffee M. W., Nishiizumi K., Wieler R., Jenniskens P., and Shaddad M. H. 2010. Cosmogenic nuclides in Almahata Sitta ureilites: Cosmic ray exposure age, preatmospheric mass, and bulk density of asteroid 2008 TC₃. *Meteoritics & Planetary Science* 45:1728–1742.
- Weyrauch M. and Bischoff A. 2012. Macrochondrules in chondrites—Formation by melting of mega-sized dust aggregates and/or by rapid collisions at high temperatures? *Meteoritics & Planetary Science* 47:2237–2250.
- Wiechert U., Halliday A., Palme H., and Rumble D. 2004. Oxygen isotope evidence for rapid mixing of the HED meteorite parent body. *Earth and Planetary Science Letters* 221:373–382.
- Wieler R. 2002. Cosmic-ray-produced noble gases produced in meteorites. *Reviews in Mineralogy and Geochemistry* 47:125–170.
- Wilkison S. L. and Robinson M. S. 2000. Bulk density of ordinary chondrite meteorites and implications for asteroidal internal structure. *Meteoritics & Planetary Science* 35:1203–1213.
- Williams N. H. 2015. The origin of titanium isotopic anomalies within solar system material. PhD thesis, The University of Manchester, Manchester, UK.
- Yamakawa A., Yamashita K., Makishima A., and Nakamura E. 2010. Chromium isotope systematics of achondrites: Chronology and isotopic heterogeneity of the inner solar system bodies. *The Astrophysical Journal* 720:20–24.
- Zhang J., Dauphas N., Davis A. M., and Pourmand A. 2011. A new method for MC-ICPMS measurement of Ti isotopic composition: Identification of correlated isotope anomalies in meteorites. *Journal of Analytical Atomic Spectrometry* 26:2197–2205.
- Zhang J., Dauphas N., Davis A. M., Leya I., and Fedkin A. 2012. The proto-Earth as a significant source of lunar material. *Nature Geoscience* 5:251–255.

SUPPORTING INFORMATION

Additional supporting information may be found in the online version of this article:

Data S1. Samples and Analytical Procedures.

Fig. S1. Modal analysis of the Stubenberg meteorite. a) SEM-BSE mosaic of sample H130,4a. b) Color-segmented phase map of the SEM-BSE mosaic indicating the different mineral phases. Pyroxenes could not be distinguished based on the BSE coefficients. c) SEM-EDX phase map of the area marked in (a). Orthopyroxene (Opx) and clinopyroxene (Cpx) are distinguished based on their Ca contents.

Fig. S2. Raman spectra of anatase (a), rutile (b), and ilmenite (c) from Stubenberg meteorite.

Fig. S3. Plot of $\delta^{17}\text{O}$ versus $\delta^{18}\text{O}$ of Stubenberg (star) in comparison with published oxygen isotope data of H, L, and LL ordinary chondrites. The results of San Carlos olivine measurements (gray-filled circles) are displayed along with the terrestrial fractionation line (solid) and the carbonaceous chondrite anhydrous minerals mixing line (dashed).

Fig. S4. The Ti isotope compositions ($\epsilon^{46}\text{Ti}/^{47}\text{Ti}$ versus $\epsilon^{50}\text{Ti}/^{47}\text{Ti}$) for various meteorite groups. Each

group occupies a unique space in the diagram. Black diamonds denote Stubenberg. Data from this study and Williams (2015).

Fig. S5. Midinfrared spectra of Stubenberg (in wavelength). Vertical lines mark characteristic features discussed in the text.

Fig. S6. Magnetic susceptibility values of representative meteorites and fragments of the Stubenberg fall with average (solid line) and confidence interval (dashed lines at ± 2 standard deviations of all measured values).

Table S1. Modal mineral abundances of the Stubenberg breccia (sample M6) obtained from EDS X-ray maps and BSE images. A = area used for image segmentation.

Table S2. Chemical composition of metals and troilite within the Stubenberg fragmental breccia. All data in wt%. n.d. = not detected; n = number of analyses.

Table S3. Concentration of primordial radionuclides (ng g^{-1} for U and Th chains and $\mu\text{g g}^{-1}$ for K_{nat}) in the specimens M1b and M5 of the Stubenberg stone measured by nondestructive gamma-ray spectroscopy. Errors include a 1 Sigma uncertainty of 10% in the detector efficiency calibration.